UNIVERSITY OF ALBERTA

A SILICA BASED INTEGRATED OPTIC MICROWAVE POWER SENSOR

BY

ALAN JULIAN PAUL HNATIW

©

A thesis submitted to the Faculty of Graduate Studies and Research in partial fulfillment of the requirements for the degree of **Master of Science**.

DEPARTMENT OF ELECTRICAL ENGINEERING

Edmonton, Alberta

Fall, 1996

National Library
of Canada

Acquisitions and
Bibliographic Services Branch

395 Wellington Street
Ottawa, Ontario
K1A 0N4

Bibliothèque nationale
du Canada

Direction des acquisitions et
des services bibliographiques

395, rue Wellington
Ottawa (Ontario)
K1A 0N4

Your file *Votre référence*

Our file *Notre référence*

The author has granted an irrevocable non-exclusive licence allowing the National Library of Canada to reproduce, loan, distribute or sell copies of his/her thesis by any means and in any form or format, making this thesis available to interested persons.

L'auteur a accordé une licence irrévocable et non exclusive permettant à la Bibliothèque nationale du Canada de reproduire, prêter, distribuer ou vendre des copies de sa thèse de quelque manière et sous quelque forme que ce soit pour mettre des exemplaires de cette thèse à la disposition des personnes intéressées.

The author retains ownership of the copyright in his/her thesis. Neither the thesis nor substantial extracts from it may be printed or otherwise reproduced without his/her permission.

L'auteur conserve la propriété du droit d'auteur qui protège sa thèse. Ni la thèse ni des extraits substantiels de celle-ci ne doivent être imprimés ou autrement reproduits sans son autorisation.

ISBN 0-612-18271-1

Canada

UNIVERSITY OF ALBERTA

RELEASE FORM

NAME OF AUTHOR:	**Alan Julian Paul Hnatiw**
TITLE OF THESIS:	**A Silica Based Integrated Optic Microwave Power Sensor**
DEGREE:	**Master of Science**
YEAR OF THIS DEGREE GRANTED:	**Fall 1996**

Permission is hereby granted to the University of Alberta Library to reproduce single copies of this thesis and to lend or sell such copies for private, scholarly or scientific purposes only.

The author reserves all other publication and except as hereinbefore provided neither the thesis nor any substantial portion thereof may be printed or otherwise reproduce in any material form whatever without the author's prior written permission.

Alan Hnatiw

8707 - 25 A Avenue
Edmonton, Alberta
Canada, T6K 2W6

DATE: Oct 3, 1996

UNIVERSITY OF ALBERTA

FACULTY OF GRADUATE STUDIES AND RESEARCH

The undersigned certify that they have read, and recommend to the Faculty of Graduate Studies and Research for acceptance, a thesis entitle **A Silica Based Integrated Optic Microwave Power Sensor** submitted by **Alan Julian Paul Hnatiw** in partial fulfillment of the requirements for the degree of **Master of Science**.

Prasad S. Apte

P. S. Apté, Co-Supervisor

R.I. MacDonald, Co-Supervisor

M. Brett, Internal Examiner

J. Harrison, External Examiner

DATE: Oct 3, 1996

For my grandparents.

ABSTRACT

A novel silica based integrated optic microwave power sensor has been designed and fabricated. The sensor operates by using the time-average microwave power, dissipated in a microwave absorbing material, to phase modulate an optical signal guided in one arm of an integrated Mach-Zehnder interferometer. The Mach-Zehnder is implemented using multimode interference couplers from ridge waveguides. The phase modulated optical signal is converted into an intensity encoded signal by the Mach-Zehnder interferometer. The optical signal is detected, processed and converted to give a measurement of microwave power. Attractive features include fabrication from low loss dielectric materials and its compact size, measuring only 5 mm by 4 mm.

Fabrication of the sensor is done using a glass-on-glass process. A dielectric waveguiding structures is created using SiO_2 and SiO_xN_y. The use of dielectric materials with low loss factors means that the sensor minimally perturbs the microwave field.

The sensing element measures 200 μm by 2 mm, and is the only material in the sensor that is not a dielectric. The sensor has been tested with microwaves at a frequency of 2.45 GHz and power levels ranging from 25 W to 1000 W. The sensor has demonstrated a response time of < 80 seconds and a dynamic range of > 30 dB.

ACKNOWLEDGMENTS

I would first like to thank my two supervisors, Dr. Prasad Apté and Dr. R. Ian MacDonald for their support throughout this project. The experiences gained from these two gentlemen have not only enlightened my understanding of science but also as a person. I also thank Dr. James McMullin for his encouragement, friendship and intellectual conversations, which are always stimulating and interesting. These gentlemen embody the true meaning of mentor.

I thank Westaim for their support by providing a scholarship and financial support for the project. Furthermore, I thank Dr. Weir for his ongoing efforts in establishing agreements among the involved institutions and supporting graduate student research.

I also thank the staff and students of Telecommunications Research Laboratories, for their moral and technical support. Special thanks to David Boertjes, Reza Paiam, Sheldon Walklin for their help and support. I also would like to give special thanks to David Clegg, Dino Corazza and Dr. Barrie Keyworth for their assistance in the lab.

I would also like to extend my gratitude to the staff at Westaim, especially, David Allen, Steve Corbin, Steve Launspach, Dr. William MacDonald and Stan Sladen. Their assistance is greatly appreciated.

I would also like to acknowledge Dr. James Broughton, Graham McKinnon and Tran Tran of Alberta Microelectronics Centre for their assistance with the fabrication of the sensor.

I would also like to thank Telecommunications Research Laboratories and Alberta Microelectronics Centre and the University of Alberta for the use of their facilities and financial support.

I also thank my parents, grandparents and family for their encouragement over the years. It is their support and guidance that has brought much meaning to this, and all my other work.

Finally, I thank my wife. Her support has meant so very much.

TABLE OF CONTENTS

1. INTRODUCTION **1**

1.1 Integrated Optics and Sensing 1

1.2 Microwave Power Measurement in Microwave Sintering Applications 6

1.3 Overview of Thesis 8

2. DESIGN AND MODELING OF SENSOR **10**

2.1 Integrated Optic Waveguides: Theory and Applications 10

2.1.1 Overview of Waveguide Theory *10*

2.1.2 Slab Waveguides *13*

2.1.3 Channel Waveguides *16*

2.1.4 The Effective Index Method *18*

2.1.5 Numerical Modeling of Waveguides and the Impact on Sensor Design *21*

2.2 Multimode Interference Couplers 28

2.2.1 Self-Imaging Theory *28*

2.2.2 Modal Propagation Analysis *30*

2.2.3 Effect of the Location of the Excitation Field on Image Formation: General, Paired and Symmetric Interference *34*

2.2.4 Fabrication and Operational Tolerances of MMI's *39*

2.2.5 Numerical Modeling of the Multimode Interference Couplers *41*

2.3 Mach-Zehnder Interferometers 43

2.4 Design and Modeling of the Susceptor 49

2.5 Conclusions 53

3. DEVELOPMENT AND EXPERIMENTS **55**

3.1 Fabrication of the Sensor 55

3.2 Optical Tests 61

3.3 Assembly of the Sensor 67

3.4 Microwave Tests 68

4. DISCUSSION OF RESULTS AND PRACTICAL CONSIDERATIONS 76

4.1 Comparison of Modeled Results to Experiments 76

4.2 Difficulties Encountered with Sensor Prototypes I and II 79

4.3 Practical Considerations Before Commercialization 81

4.4 Future Work and Directions 83

5. CONCLUSION 87

REFERENCES 88

APPENDIX I 94

LIST OF TABLES

TABLE 2.1 SUMMARY OF MMI PROPERTIES. 39

LIST OF FIGURES

FIGURE 1.1 CONCEPTUAL DRAWING OF THE INTEGRATED OPTIC MICROWAVE POWER SENSOR. 9

FIGURE 2.1 REFRACTIVE INDEX PROFILE OF A SLAB WAVEGUIDE..... 13

FIGURE 2.2 PERSPECTIVE DRAWING OF A SLAB WAVEGUIDE STRUCTURE. 14

FIGURE 2.3 CROSS SECTIONS OF VARIOUS CHANNEL WAVEGUIDE STRUCTURES..... 17

FIGURE 2.4 ELECTRIC FIELD DISTRIBUTION IN A STRIP-LOADED CHANNEL WAVEGUIDE. 17

FIGURE 2.5 STEP 1, DEFINE REGIONS THAT ARE SLAB LIKE WAVEGUIDES. 19

FIGURE 2.6 STEP 2, DETERMINE SLAB MODES IN EACH REGION. 19

FIGURE 2.7 STEP 4, REPLACE CHANNEL GUIDE WITH A SLAB GUIDE USING THE CALCULATED EFFECTIVE INDICES..... 20

FIGURE 2.8 CONTOUR PLOT PRODUCED BY FWAVE ILLUSTRATES THE TE FIELD DISTRIBUTION IN THE SINGLE MODE RIDGE WAVEGUIDE USED IN THE SENSOR..... 23

FIGURE 2.9 CONTOUR PLOT SHOWING THE TE FIELD DISTRIBUTION FOR THE 5 TE MODES THAT ARE SUPPORTED INSIDE A MULTIMODE INTERFERENCE COUPLER. 23

FIGURE 2.10 FLOWCHART FOR FDTD PROGRAM. 27

FIGURE 2.11 FIELD DISTRIBUTION AS DESCRIBED BY Φ_V IN A MMI 12 µM WIDE (MODE 0 THROUGH 4). 32

FIGURE 2.12 SHAPE OF THE ELECTRIC FIELD DISTRIBUTION IN THE X-DIRECTION ALONG THE LENGTH OF THE MMI AS CALCULATED BY THE PMA..... 33

FIGURE 2.13 LATERAL LOCATION OF INPUT WAVEGUIDE FOR GENERAL INTERFERENCE..... 34

FIGURE 2.14 LOCATION OF INPUT GUIDE FOR PAIRED INTERFERENCE..... 35

FIGURE 2.15 LOCATION OF INPUT GUIDE FOR SYMMETRIC INTERFERENCE. 35

FIGURE 2.16 MIRROR IMAGE OF INPUT FIELD OR COUPLER OPERATING IN THE CROSS STATE (THE VERTICAL LINE ILLUSTRATES THE 3 DB LENGTH, $z \cong 360\ \mu m$). 37

FIGURE 2.17 COMPARISON OF GENERAL (A) AND SYMMETRIC (B) MMI COUPLERS.38

FIGURE 2.18 REFRACTION STEP OF A BPM IS EQUIVALENT TO PROPAGATING THE FIELD THROUGH A LENS. 42

FIGURE 2.19 BPM SIMULATION OF THE ENTIRE SENSOR..... 43

FIGURE 2.20 SOME COMMON TYPES OF INTERFEROMETERS. 44

FIGURE 2.21 CONCEPTUAL DRAWING OF AN INTEGRATED MACH-ZEHNDER INTERFEROMETER. 45

FIGURE 2.22 INTENSITY RESPONSE OF A MZ TO A TEMPERATURE DIFFERENTIAL. ... 48

FIGURE 2.23 HEAT FLOW IN THE SENSOR CALCULATED USING PDEASE. 52

FIGURE 2.24 CONTOUR PLOT OF THE TEMPERATURE DISTRIBUTION WHEN THE SUSCEPTOR IS HEATED BY 100 W OF MICROWAVE POWER. 53

FIGURE 3.1 SEM PICTURE OF MMI COUPLER PROTOTYPE I (OUTPUT END)..... 59

FIGURE 3.2 SEM PICTURE OF MMI COUPLER PROTOTYPE II AND PART OF THE MZ ARMS. 60

FIGURE 3.3 SEM PICTURE OF THE SIDEWALL ROUGHNESS OCCURRING ON THE WAVEGUIDE SIDES (PROTOTYPE I). 60

FIGURE 3.4 OPTICAL TEST SETUP. 63

FIGURE 3.5 TEST SETUP FOR MEASUREMENT OF PROPAGATION LOSS USING THE OUT-SCATTER METHOD AND A MULTIMODE FIBRE. 65

FIGURE 3.6 SETUP FOR DETERMINE THE IMBALANCE OF THE MACH-ZEHNDER. 66

FIGURE 3.7 DRAWING OF ASSEMBLED SENSOR. FOR A DETAILED DRAWING OF THE SENSOR SEE FIGURE 2.21 67

FIGURE 3.8 PICTURE OF SENSOR PROTOTYPE II. 68

FIGURE 3.9 MICROWAVE TEST SETUP. 69

FIGURE 3.10 ENLARGED VIEW OF THE TE_{10} MICROWAVE APPLICATOR. 69

FIGURE 3.11 TOP-VIEW OF THE MICROWAVE APPLICATOR SHOWING THE TWO DIFFERENT SENSOR ORIENTATIONS TESTED 71

FIGURE 3.12 RESPONSE OF SENSOR PROTOTYPE II TO MICROWAVE POWER WHEN TILTED PERPENDICULAR TO THE DIRECTION OF MICROWAVE POWER FLOW. NOTE: THE PLOT FOR OUTPUT 2 WAS SHIFTED UP BY 40 DBM. 73

FIGURE 3.13 RESPONSE OF PROTOTYPE II TO MICROWAVE POWER WHEN TILTED PARALLEL TO THE DIRECTION OF MICROWAVE POWER FLOW. NOTE: THE PLOT FOR OUTPUT 2 WAS SHIFTED UP BY 40 DBM. 74

FIGURE 3.14 RESPONSE OF SENSOR PROTOTYPE I TO MICROWAVE POWER (OUTPUT 2 WAS NOT FUNCTIONAL). 75

FIGURE 3.15 RESPONSE TIME OF PROTOTYPE II TO A 50 WATT CHANGE IN MICROWAVE POWER (POWER SETPOINT WAS 200 W)..... 75

FIGURE 4.1 COMPARISON BETWEEN MODELED AND EXPERIMENTAL RESULTS USING THE MZ TRANSFER FUNCTION EQUATION..... 78

FIGURE 4.2 IMPROVED METHOD OF BUTT COUPLING THE FIBRES TO THE WAVEGUIDES. 82

FIGURE 4.3 INTENSITY AT THE OUTPUT OF A 2X4 MMI COUPLER. 85

1. INTRODUCTION

1.1 Integrated Optics and Sensing

Over the past 25 years optical sensing has been maturing, much like the telecommunications industry. Actually, it is the telecommunication industry's relentless progress in manufacturing higher quality components at an ever decreasing cost that has advanced optical sensing technology. Laser diodes with narrow linewidths, low noise figures and long life spans as well as improvements in other components, have made possible practical optical sensing products that can compete with conventional sensing technologies. During the past 10 years there has been a shift away from discrete fibre sensors or bulk optic sensors to integrated sensors, which combine many optical components, such as splitters and waveguides, on a common substrate.

The subject of integrated optics is both vast and complex, however, integrated optics generally seeks to miniaturize bulk optical circuits, much as discrete electrical circuits have been miniaturized by microelectronics. More specifically, there are two types of optical integration: monolithic and hybrid. Monolithic integration, whereby devices, such as laser, waveguides and detectors, can be made from similar materials (usually semiconductors) fabricated on a common substrate, is the most difficult but has the most

potential. Monolithic integration is very complicated since materials that have complementary properties, such as detectors which must absorb light and waveguide which must be transparent, must be fabricated together. Although the packing densities and size attributes of monolithic integration are attractive, the technology must be advanced much further before complicated monolithic optical devices are practical.

At present, hybrid integration allows optimization of the materials required for various functions. With hybrid integration, discrete devices in chip form are mounted onto a common substrate. Optical waveguides make use of the substrate as part of the waveguiding structure to interconnect the discrete components. Electrically conducting paths for signaling and biasing certain components can be accomplished by metallization of the same substrate. Thus, hybrid integration uses devices that have been fabricated separately using optimized processes, and integrates them on common substrate as a single package. The benefits in reduced power consumption and size are immediately obvious when one considers a hypothetical device created using either bulk, hybrid or monolithic integration. A typical bulk optical device may occupy one square metre of space on an optical table. A similar device assembled using hybrid integration may occupy a few square centimetres, and in turn, a monolithic device may only occupy a few tens of square millimetres (excluding the necessary power supplies). It is this drive

to miniaturize and integrate functionality onto a single "chip" that has resulted in increased reliability and reduced cost. Hence, these future integrated optical devices will therefore have the greatest impact in the marketplace.

Often in an optical communications system, it is necessary to reduce the impact of environmental influences, such as temperature, strain and pressure. However, the goal in designing a sensor or sensing system is to capitalize on one of these external influences to maximize sensitivity. The function of a sensor is to convert energy from one form to another. The energy form which is being measured is called the measurand and the energy form to which it is converted is called the signal. The conversion of the measurand to a detectable signal, called the transduction mechanism, must be maximized and exploited. Fibre optic sensors are capable of detecting a variety of measurands, which can be classified in six general categories [1]: radiant, mechanical, thermal, electrical, magnetic, and chemical. Microwave energy is a radiant form of energy, and it is microwave power which is detected by the microwave power sensor discussed in this thesis.

The transduction mechanism is usually an indirect or multi-stage conversion of the measurand to the information signal. Most transduction mechanisms for optical sensors are indirect, whereas most other sensor types use a direct transduction mechanism. For instance, the potential across a

thermocouple is a direct result of temperature, and can be well characterized. Often, it is difficult to eliminate all external influence which can cause subtle variations in an optical sensor. Therefore, for optical sensors, the transduction mechanism must be well understood and carefully implemented.

The transduction mechanism is what modulates or encodes the optical signal. The microwave power sensor incorporates a multi-stage transduction process. Microwave energy is absorbed by a susceptor or microwave absorbing material. The absorbed energy is converted to heat, which creates a temperature gradient. This temperature gradient causes a differential change in the refractive indices of two waveguides. This change in the refractive index modulates the phase of two light signals. When the signals are recombined the phase difference is converted to an intensity signal which can then be calibrated to microwave power and used as a microwave power sensor.

Fibre optic sensors have many advantages over their electrical counterparts. The advantages can be separated into two categories: attractive features that are unique to optical sensors, and features which are common among different types of sensors, which are improved using optical sensors. Some of the features that are unique (or nearly unique) to optical sensors are: immunity to EMI (electromagnetic interference), electrical isolation, inability

to cause sparks or ignite volatile substances, ultra-wide bandwidth, ability to operate in high temperature environments and readily multiplexed together to ease distribution. Other attractive features of optical sensors are: small size and weight, chemically inert, high sensitivity and large dynamic range.

Both optical and electrical types of microwave power sensors exist in the market and in research laboratories [2-5]. However, some disadvantages of current sensors are: large size, metal components, limited power range and high cost. The main advantages of the optical microwave power sensor are that it detects the time averaged power eliminating the need for expensive radio frequency devices found in other systems, and it minimally perturbs the microwave field. As a result, the optical microwave power sensor is ideally suited to applications where multimode cavity applicators are used to process materials [6-7].

Optical sensors are fabricated entirely out of dielectrics and therefore minimally perturb the field to be measured. The optical microwave power sensor uses a Mach-Zehnder interferometer to coherently interfere two light beams in order to produce an intensity signal that is dependent upon their optical phase difference. A balanced Mach-Zehnder interferometer is used, which is insensitive to influences common to the two light paths. This is very important, since the temperature gradient caused by the absorption of microwave energy by the susceptor modulates the optical phase. Without a

balanced Mach-Zehnder design, ambient temperature effects would also modulate the optical phase.

1.2 Microwave Power Measurement in Microwave Sintering Applications

The microwave power sensor was originally designed and intended for use in applications where microwaves are used to sinter ceramic materials. The process of sintering ceramic materials relies on the generation of heat caused by the absorption of microwave power by the ceramic powders. The microwave power is delivered by a microwave applicator, which is often a resonant multimode metal cavity. In order to heat the material efficiently, it must be surrounded by insulation. Once the powders achieve a sufficiently high temperature they begin to chemically react to form the desired composite ceramic material. The process is complicated by the fact that different materials have a temperature dependent microwave loss factor or loss tangent. As the powders heat they become more lossy and couple with the microwave field more efficiently, thereby heating faster as they get hotter. If this process is not carefully balanced by heat loss and control of the microwave power, localized heating will occur and result in thermal runaway. The loss factor can increase by an order of magnitude in under a second when the material enters thermal runaway. At this point the materials often melt or decompose and are useless.

The process of microwave heating can be controlled by monitoring either the temperature of the materials or the microwave field distribution inside the microwave applicator. There are a limited number of sensors that can be used to monitor the temperature inside a microwave applicator because of the high temperatures that are involved in sintering and the presence of the microwave field. The most common sensors are: thermocouples, light pipes and blackbody probes. Thermocouples can only be effectively used by turning off the microwave source, otherwise they would cause arcing due to their metallic composition. The obvious disadvantage is that the temperature cannot be monitored in real time, nor can it be accurately measured because once the source of microwaves is terminated the temperature of the material drops rapidly. Temperature measurement using light pipes and blackbody probes rely on the emission of light by the materials. Since the theory regarding the radiation of light is well understood, an accurate measurement can be made. However, unless the emissivity of the material is known as a function of temperature only an estimate of the temperature or a relative measurement can be made. Other techniques which measure the radiation at two or more wavelengths can be used to determine the emissivity and therefore the temperature. The major drawbacks of these two sensors are: high system cost (typically > $30,000 for the controller and $5,000 for each sensor), fragility and large size. The optical

microwave power sensor was designed to overcome these limitations and issues.

The optical power sensor is small, measuring approximately 5 mm by 4 mm, is relatively inexpensive (<10,000 for laser, detector and sensor) and minimally perturbs the microwave field due to its construction from low loss dielectric materials. Furthermore, the temperature uniformity can be determined by monitoring the distribution of the microwave field from the low temperature side of the insulated object. Therefore, the sensor need only operate in ambient temperatures of <600°C. Hot spots in the material can be determined by the presence of peaks in the time-averaged power distribution gathered by the sensor just outside the insulating layer(s). By using the optical microwave power sensor, sintering of ceramics can be controlled more accurately, which reduces the possibility of hot spot formation and thermal runaways.

1.3 Overview of Thesis

It was the goal of this project to not only develop a new sensor for a specific application, but one that could be rugged, robust and cost effective. A conceptual drawing of the optical microwave sensor is shown in Figure 1.1. The theory regarding the operation of the main components which are part of the sensor, such as waveguides, splitters, Mach-Zehnder interferometer and the susceptor, will be presented.

In Chapter 2 the design of the sensor will be discussed. Specifically, the theory used to design the waveguides, multimode splitters, Mach-Zehnder interferometer and susceptor will be examined. Results of numerical simulations will be given and discussed.

The fabrication of the device is presented in Chapter 3. The materials used and steps taken to ensure a high quality optical device will be discussed. Also, the tests done to evaluate the fabricated sensor will be presented.

The analysis and interpretation of the data collected will be discussed in Chapter 4. Experimental results will be compared to the modeled results and conclusions about the merit of the models will be drawn. The future direction of the sensor and areas for improvement will also be discussed.

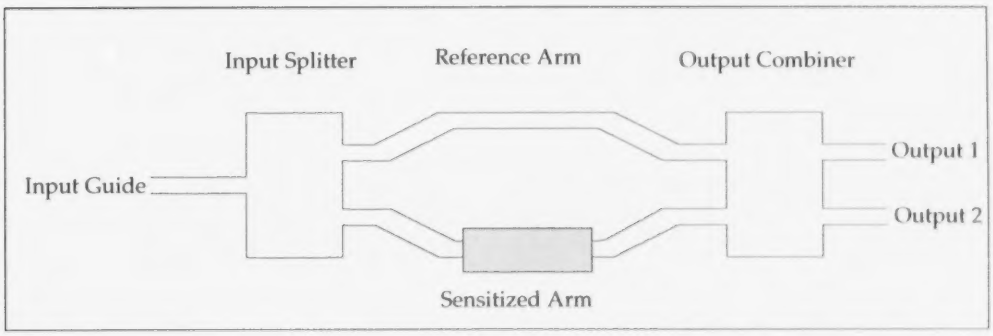

Figure 1.1 Conceptual drawing of the integrated optic microwave power sensor.

2. DESIGN AND MODELING OF SENSOR

Successive refinements were made in the sensor design throughout the course of this work, resulting in the fabrication of three prototypes. The knowledge gained from each design iteration was incorporated into the ensuing prototypes. This chapter will present the steps involved and theory necessary to design the sensor.

2.1 Integrated Optic Waveguides: Theory and Applications

Integrated optics is concerned with the miniaturization and combination of optical components into a single functional unit, much like current integrated electronic circuits. In order to connect these components, optical waveguides, analogous to wires, are used. Integrated optical waveguides fall into the general class of dielectric waveguides. Currently, the most common dielectric waveguide is glass optical fibre, used extensively in telecommunications and high bandwidth computer networks. The design of the sensor required integrated optic waveguides. In this section the theory governing the design of 2-D slab waveguides and 3-D channel waveguides will be presented.

2.1.1 Overview of Waveguide Theory

The theory behind the propagation of electromagnetic waves through a waveguide structure has been studied in great detail [8-9]. Here a brief

overview of the equations which describe the propagation of electromagnetic waves will be discussed.

Our starting point in the development of waveguide theory is Maxwell's time dependent equations (2.1),

$$\nabla \times \vec{\mathcal{H}} = \varepsilon_o \varepsilon_r \frac{\partial \vec{\mathcal{E}}}{\partial t} \tag{2.1a}$$

$$\nabla \times \vec{\mathcal{E}} = \mu_o \mu_r \frac{\partial \vec{\mathcal{H}}}{\partial t} \tag{2.1b}$$

where μ_o is the magnetic permeability of free space, μ_r is the relative magnetic permeability of the material to free space, ε_r is the relative electric permittivity to free space, ε_o is the electric permittivity of free space, and $\vec{\mathcal{E}}$ and $\vec{\mathcal{H}}$ are the time varying electric and magnetic vector fields. If the electromagnetic wave is monochromatic, then the electric and magnetic fields are harmonic functions of time with a single frequency given by:

$$\vec{\mathcal{E}}(x,y,z,t) = \vec{E}(x,y,z)e^{j\omega t} \tag{2.2a}$$

$$\vec{\mathcal{H}}(x,y,z,t) = \vec{H}(x,y,z)e^{j\omega t} \tag{2.2b}$$

Substituting the above equations into (2.1), the following equations for an isotropic homogenous medium which contains no free charges or currents are obtained:

$$\nabla \times \vec{H} = j\omega\varepsilon_o \varepsilon_r \vec{E} \tag{2.3a}$$

$$\nabla \times \vec{E} = -j\omega\mu_o \mu_r \vec{H} \tag{2.3b}$$

Taking the curl of (2.3b), then making use of a vector identity and substituting (2.3a), leads to the time independent wave equation, or Helmholtz's equation,

$$\nabla^2 \vec{E} + \omega k^2 \vec{E} = 0 \tag{2.4}$$

where

$k = \dfrac{\omega}{\sqrt{\varepsilon_r \varepsilon_o \mu_o}} = \dfrac{2\pi}{\lambda} = nk_o$ is the wavenumber of the propagating wave

n is the refractive index of the medium, and

k_o is the wavenumber in free space.

Up to this point little has been assumed about the direction of propagation. For the rest of this thesis it shall be assumed that the EM wave is propagating in the z-direction. Furthermore, if the wave amplitudes varies slowly as a function of z within a waveguide, then the z dependency can be factored out as shown below for the electric field,

$$\vec{E}_m(x, y, z) = \vec{E}_m(x, y) e^{j\beta_m z} \tag{2.5}$$

where $\vec{E}_m$ represents multiple solutions which satisfy the wave equation and β_m is the propagation constant for the m^{th} mode. The task now at hand is to find the field distribution $\vec{E}_m(x, y)$. Unless the geometry of the waveguide structure is simple (i.e. rectangular or circular) numerical methods must be used to solve the equations. However, slab guides can be solved analytically and three-dimensional channel guides can be approximated as slab guides

when certain approximations and modifications are applied.

2.1.2 Slab Waveguides

Many integrated optic devices can be approximated by slab waveguides because light in them is weakly guided in one direction and strongly guided in the other transverse direction. In this section slab waveguide structures will be discussed. In the following section, slab waveguide theory will be extended to account for two-dimensional channel waveguides more generally.

Slab waveguides are characterized by three or more layers of dielectric materials which guide light in one transverse direction, while allowing it to diffract naturally in the other direction. This implies that the refractive index profile at any distance z along the waveguide is dependent only on x, i.e. n=n(x). Figure 2.1 illustrates a typical slab waveguide refractive index profile.

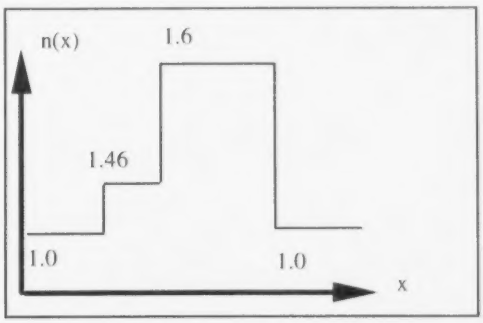

Figure 2.1 Refractive index profile of a slab waveguide.

As previously mentioned, light is assumed to propagate in the z-direction. Figure 2.2 shows a perspective drawing of a slab waveguide structure with the electric field distribution of the fundamental mode superimposed.

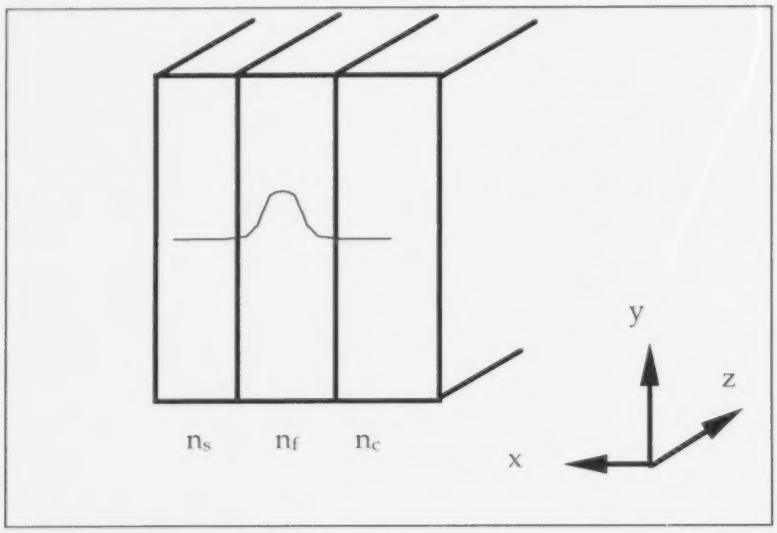

Figure 2.2 Perspective drawing of a slab waveguide structure.

In Figure 2.2, $n_f > n_s, n_c$. The refractive index of the core or film layer is n_f, and the refractive indices of the substrate and cladding layers are n_s and n_c respectively. Often the cladding layers is air ($n_c \cong 1.0$), so only two materials must be chosen to fabricate the waveguide.

The modes that can propagate in the waveguide are known as eigenmodes or guided modes. We can define modes of two polarizations; the transverse electric field mode, TE, and the transverse magnetic field mode, TM. Since the equation governing both polarizations are similar, with the exception of the boundary conditions and a few constants, only TE modes

will be discussed. The electric field distribution for guided modes in slab waveguides have exponentially decaying tails in the cladding regions and a sinusoidal form in the core region. The electric field distribution, $E_m(x)$, for all propagating modes can be expressed as,

$$E_m(x) = \begin{cases} A_s e^{\gamma_s (x+a)} & x < -a \\ A_f \cos(\kappa_f x + \phi_s) & -a < x < a \\ A_c e^{-\gamma_c (x-a)} & x > a \end{cases} \tag{2.6}$$

where $2a$ represents the width of the core, κ_f is the transverse component of the propagation constant in the film, γ_c and γ_s are the field strength decay constants in the cladding and substrate and the A_s, A_f and A_c are proportional to the field amplitude. All of these constants are chosen to satisfy continuity of the field and its derivatives at $x=\pm a$. The entire field, $E(x,z)$, at any distance along the z-axis is given by the sum of M propagating modes:

$$E(x,z) = \sum_{m=0}^{M-1} \hat{E}_m(x) e^{j\beta_m z} \tag{2.7}$$

where it has been assumed that each m mode has been power normalized according to:

$$\hat{E}_m = \frac{E_m(x)}{\int_{-\infty}^{+\infty} |E_m(x)|^2 \, dx} \tag{2.8}$$

Equation (2.7) can be used to determine the magnitude and phase of the field at any location in (x,z) space.

Thus far only guided or propagating modes have been discussed, however, radiation modes can also exist. These modes are not guided and are a source of power loss. Whereas the fields of guided modes have a sinusoidal distribution in the core and an exponential shape in the cladding, radiation modes have sinusoidal distributions in one or both cladding regions. These modes are often excited when light from a fibre is coupled to a slab or when the slab structure is bent or curved. When designing waveguide structures stimulation of these radiation modes should be avoided.

2.1.3 Channel Waveguides

Unlike slab guides where the field is only confined in one direction, channel waveguides confine the field in both the x and y directions. The field is guided in the vertical direction similar to a slab waveguide, but a strip or ridge is often formed in the horizontal direction to provide the required index variation for guided wave propagation.

Figure 2.3 shows a number of channel waveguide structures and Figure 2.4 shows the electric field distribution in a strip-loaded single mode guide.

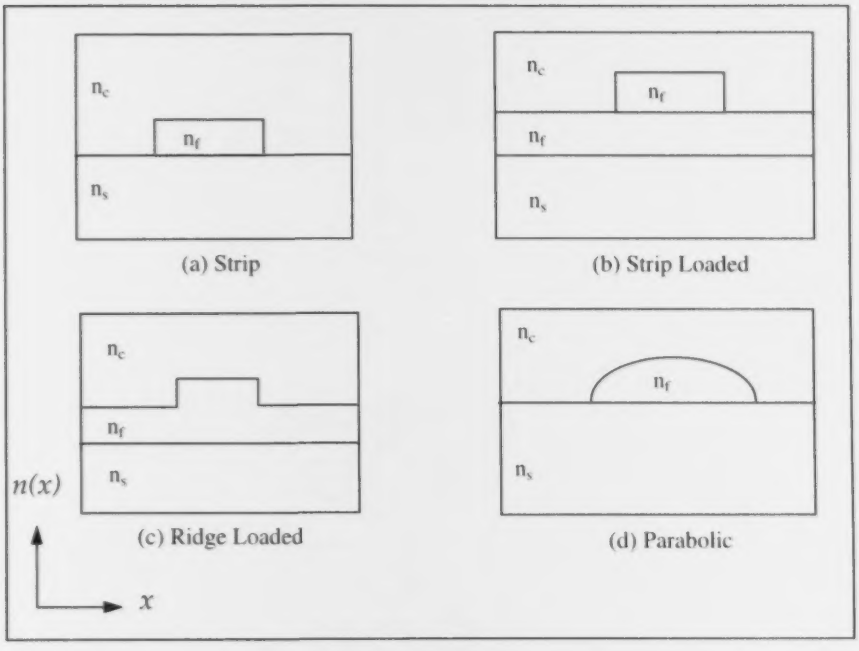

Figure 2.3 Cross Sections of various channel waveguide structures.

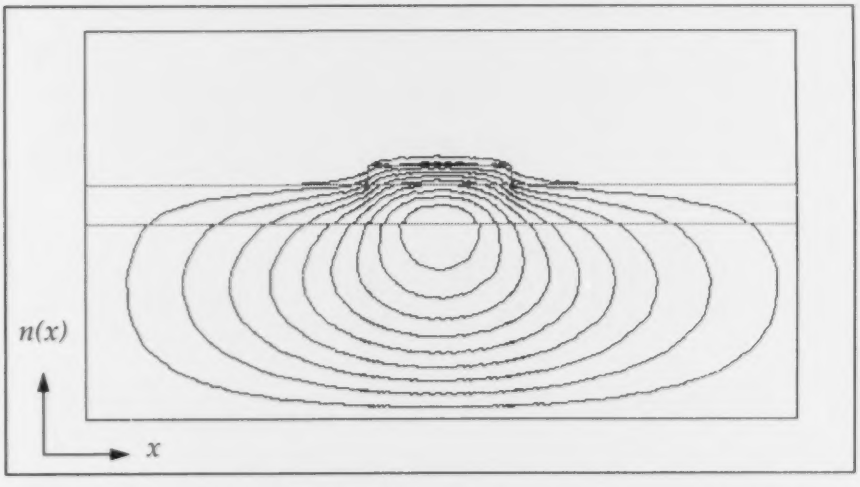

Figure 2.4 Electric field distribution in a strip-loaded channel waveguide.

In Figure 2.3, n_f is the film or core index, n_c is the cladding index and n_s in the index of the substrate. Ridge waveguides are very popular because of their

ease of fabrication and versatility. These guides are fabricated by depositing the film layer on the substrate using a variety of film deposition techniques, such as CVD (chemical vapour deposition), flame hydrolysis, etc. [10-11]. To create the ridge, the film layer is masked with photoresist and then unexposed areas of the film are etched. Dry etching techniques, such as reactive ion etching, are becoming more popular because of their ease of use, versatility, and their ability to etch anisotropically [12].

Since the index profiles may be complex, channel waveguides are difficult to analyze analytically. As a result, the electric field distributions for channel waveguides are often determined numerically. Some numerical methods use mode solvers and beam propagation methods, and will be discussed in later sections. However, there is one very important analytic method, the effective index method (EIM), which approximates a channel waveguide by a slab guide [13-15]. A great deal of insight can be gained by studying waveguides using the EIM, which is presented in the next section.

2.1.4 The Effective Index Method

The EIM is analogous to the reduction of a 2-D partial differential equation (PDE) to an ordinary differential equation (ODE) or the reduction of a 3-D PDE to a 2-D PDE. In other words, the number of dimensions of the problem is reduced by one. The steps involved in implementing the method are:

1. to break the channel waveguide structure into local regions that are slab guides (see Figure 2.5)
2. to solve for the slab mode(s) in each region (see Figure 2.6)
3. to calculate an effective refractive index, n_{eff}, given by $n_{eff} = \frac{\beta_m}{k_o}$

to replace each region with a uniform effective index (Figure 2.7)

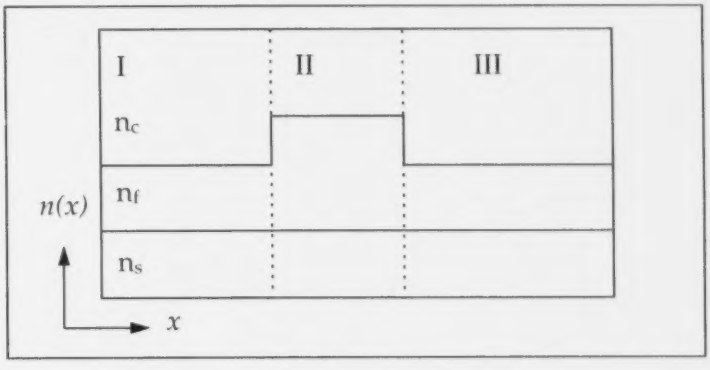

Figure 2.5 Step 1, define regions that are slab like waveguides.

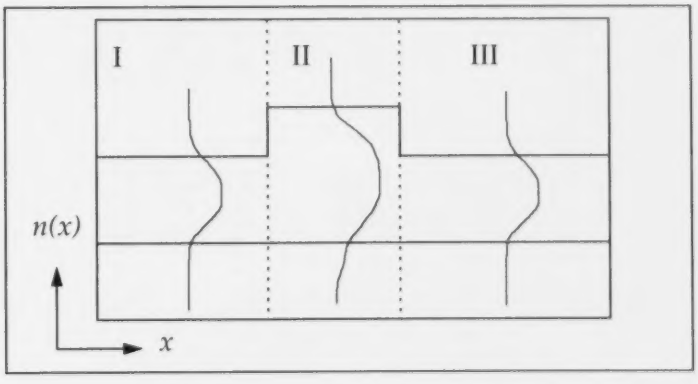

Figure 2.6 Step 2, determine slab modes in each region.

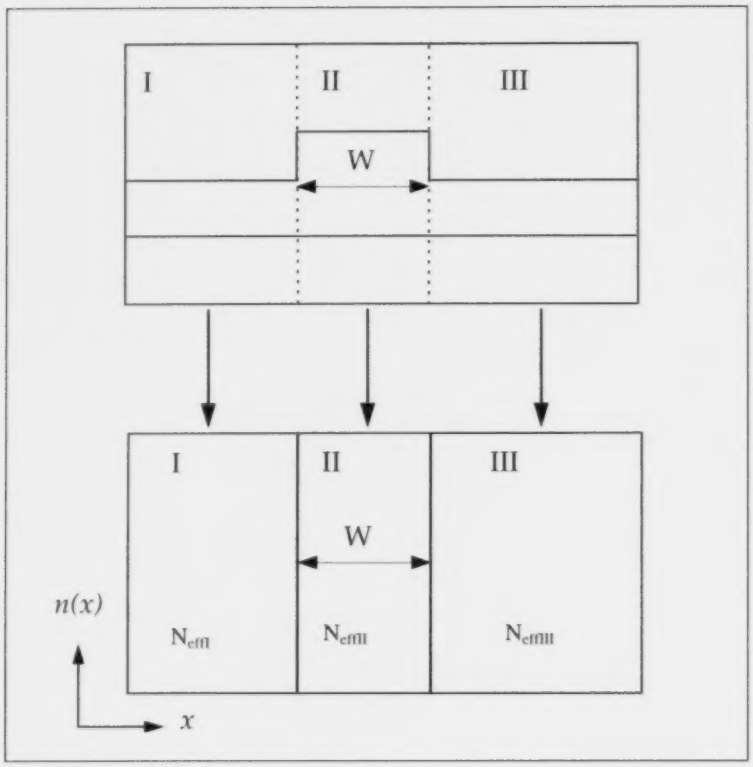

Figure 2.7 Step 4, Replace channel guide with a slab guide using the calculated effective indices.

Figure 2.7 represents a slab waveguide approximation of the original channel waveguide. The horizontal field distribution and the number of modes in the x-direction can now be solved for using equations (2.6) - (2.8). If more than one mode exists in the vertical direction, then the EIM must be re-applied for each vertical mode, because each vertical mode will give a different effective index.

Another important use of the EIM is to reduce the amount of calculation that must be done when solving problems numerically. Instead of solving a 3-D problem, the index profile is simplified via the EIM to a 2-D problem. The small error introduced by making this approximation is justified with the decrease in computer storage and execution time. The EIM was used to simplify the 3-D problem into a 2-D problem which was then solved using a 2-D BPM (beam propagation method) program. Data from the BPM simulations and an explanation of the BPM will be presented in Sections 2.2.3 through 2.2.5.

2.1.5 Numerical Modeling of Waveguides and the Impact on Sensor Design

There are a variety of numerical methods that can be used to determine the field distribution and the number of modes in channel waveguides [16-17]. Finite difference algorithms, finite element, eigenmode solvers or a combination of the above may be used to determine the fields. Furthermore, some methods only solve the scalar wave equation, while others solve the vector wave equation for the quasi-TE and quasi-TM modes. Advantages of solving the vector wave equation are; the complete field solution is available and the impact of effects, such as polarization, birefringence, etc., on the design can be investigated.

In this work, a public domain software program, FWave, for the

Macintosh computer was used [18]. It presents a user friendly interface and is powered by an adaptive finite difference mode solver which can solve either the scalar or vector wave equations for the electric field distribution. This program was used to determine the 2-D field distribution (i.e. the field at any point along the direction of propagation) for both the single mode waveguides and the modes in the multimode couplers. Furthermore, the propagation constant for each mode is given. Using this data, the length to make a 3 dB or equal output multimode splitter was determined.

Contour plots of the field distribution were generated by FWave in order to present information as concisely as possible. Figure 2.8 shows the field distribution for the single mode ridge waveguide used in the sensor and Figure 2.9 illustrates the field distribution for the modes that exist in the multimode interference coupler, which for now can be thought of as merely a multimode waveguide (multimode interference couplers will be discussed in detail in Section 2.2).

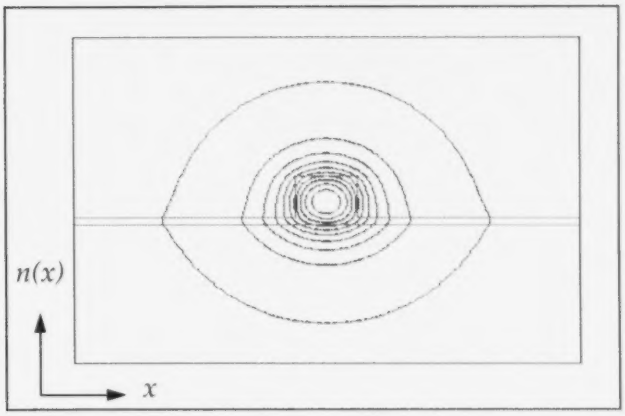

Figure 2.8 Contour plot produced by FWave illustrates the TE field distribution in the single mode ridge waveguide used in the sensor.

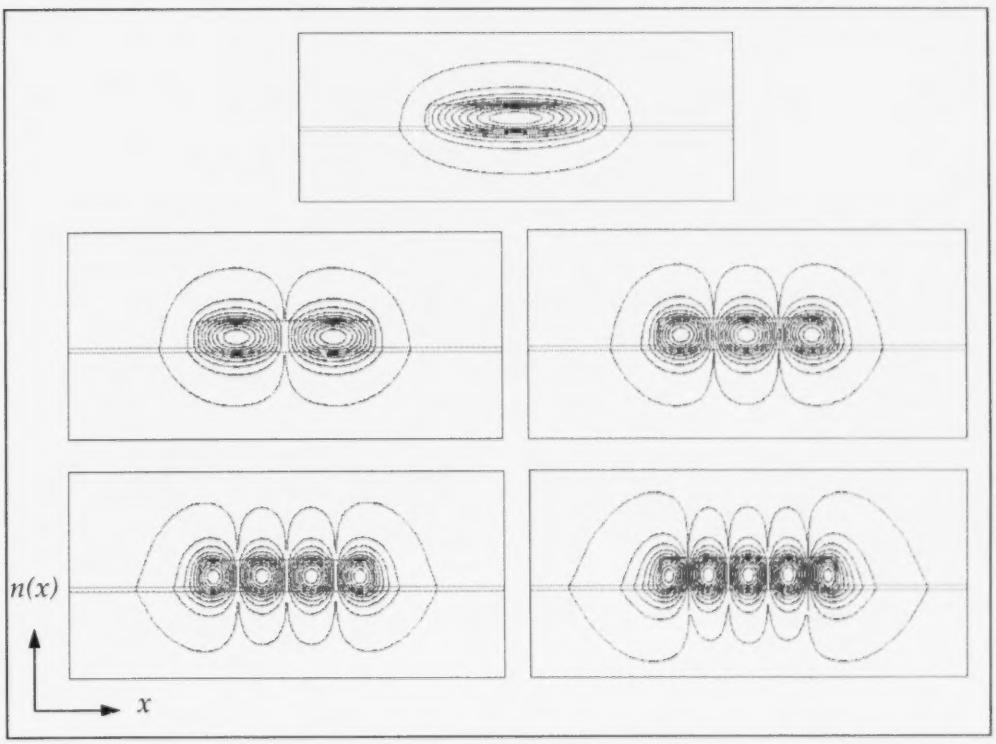

Figure 2.9 Contour plot showing the TE field distribution for the 5 TE modes that are supported inside a multimode interference coupler.

FWave was used to determine the field distribution in the buried ridge waveguides. More importantly, it was used as a feedback mechanism in the design stage to investigate alternative designs. It was possible to simulate a variety of waveguide structures quickly and choose the best design based on polarization insensitivity, high field confinement, single mode operation and ease of fabrication.

When the waveguides, S-bends and curves were designed for the sensor, it was important to obtain an estimate of the propagation losses in these structures. This could not be done using FWave and in the case of the 180° arcs, it was impossible to use other methods such as beam propagation. As a result, a finite difference time domain (FDTD) program was developed to investigate the losses of waveguide structures that involve large angles [19-21].

The FDTD method has many advantages over existing modeling programs, such as beam propagation modeling software, most notably the ability to model waveguides that have large bend angles or even guides that follow a circular arc. Furthermore, the algorithm provides other information such as reflections at interfaces and transient analysis. The algorithm is able to provide this information because it solves Maxwell's coupled partial differential equations in the time domain, rather than assuming a harmonic

solution. The tradeoff for acquiring this extra information is increased program execution time and computer memory requirements.

The FDTD method requires storing three arrays which represent the E_z, H_x and H_y fields at every grid point inside the solution domain for quasi-TE modes (or E_x, E_y and H_z for quasi-TM modes). Due to a stability condition by the solution method, the grid size should be at least one fifth of the wavelength of light inside the highest index material to insure accurate modeling (often $\lambda/10$ or $\lambda/20$ is used for improved accuracy).

As previously mentioned, the method involves solving Maxwell's coupled PDE's in the time domain, equation (2.1). If the refractive index profile is constant along the z-axis (i.e. a slab waveguide structure), implying that $\frac{\partial}{\partial z} = 0$, then equation (2.1) can be split into two sets of coupled PDE's. Equation (2.9) represents the TE solutions,

$$\begin{aligned} \frac{\partial H_x}{\partial t} &= -\frac{1}{\mu}\frac{\partial E_z}{\partial y} \\ \frac{\partial H_y}{\partial t} &= \frac{1}{\mu}\frac{\partial E_z}{\partial x} \\ \frac{\partial H_y}{\partial x} - \frac{\partial H_x}{\partial y} &= \varepsilon\frac{\partial E_z}{\partial t} + \sigma E_z \end{aligned} \tag{2.9}$$

and equation (2.10) represents the TM solutions.

$$\frac{\partial H_z}{\partial y} = \varepsilon \frac{\partial E_x}{\partial t} + \sigma E_x$$
$$\frac{\partial H_z}{\partial x} = -\varepsilon \frac{\partial E_y}{\partial t} + \sigma E_y \qquad (2.10)$$
$$\frac{\partial E_y}{\partial x} - \frac{\partial E_x}{\partial y} = -\mu \frac{\partial H_z}{\partial t}$$

Therefore, E_z, H_x and H_y are related through three coupled partial differential equations, as are H_z, E_x and E_y.

Accounting for the TE modes only, (2.9) is solved by replacing the derivatives with central finite differences which results in an explicit finite difference solution scheme given by:

$$H_x^{n+\frac{1}{2}}(i, j+\tfrac{1}{2}) = H_x^{n-\frac{1}{2}}(i, j+\tfrac{1}{2}) + \frac{\Delta t}{\mu(i, j+\frac{1}{2})}\left[\frac{-E_z^n(i, j+1) + E_z^n(i, j)}{\Delta y}\right]$$

$$H_y^{n+\frac{1}{2}}(i+\tfrac{1}{2}, j) = H_y^{n-\frac{1}{2}}(i+\tfrac{1}{2}, j) + \frac{\Delta t}{\mu(i+\frac{1}{2}, j)}\left[\frac{E_z^n(i+1, j) - E_z^n(i, j)}{\Delta x}\right] \qquad (2.11)$$

$$E_z^{n+1}(i, j) = \left[1 - \frac{\sigma(i, j)\Delta t}{\varepsilon(i, j)}\right] E_z^n(i, j) + \frac{\Delta t}{\varepsilon(i, j)} \cdot$$
$$\left[\frac{H_y^{n+\frac{1}{2}}(i+\frac{1}{2}, j) - H_y^{n+\frac{1}{2}}(i-\frac{1}{2}, j)}{\Delta x} + \frac{-H_x^{n+\frac{1}{2}}(i, j+\frac{1}{2}) + H_x^{n+\frac{1}{2}}(i, j-\frac{1}{2})}{\Delta y}\right]$$

where n represents the time step index, i and j are the two spatial indices, Δx and Δy are the spatial increments in the x and y-directions, σ is the conductivity, μ is the permeability of the material and ε is permittivity of the material. The equations are solved by time-stepping through the algorithm

and evaluating the E and H components at alternate half-time steps, i.e. for each loop or time step, the new values of H are used to determine E. Figure 2.10 shows a flowchart illustrating how the method is executed.

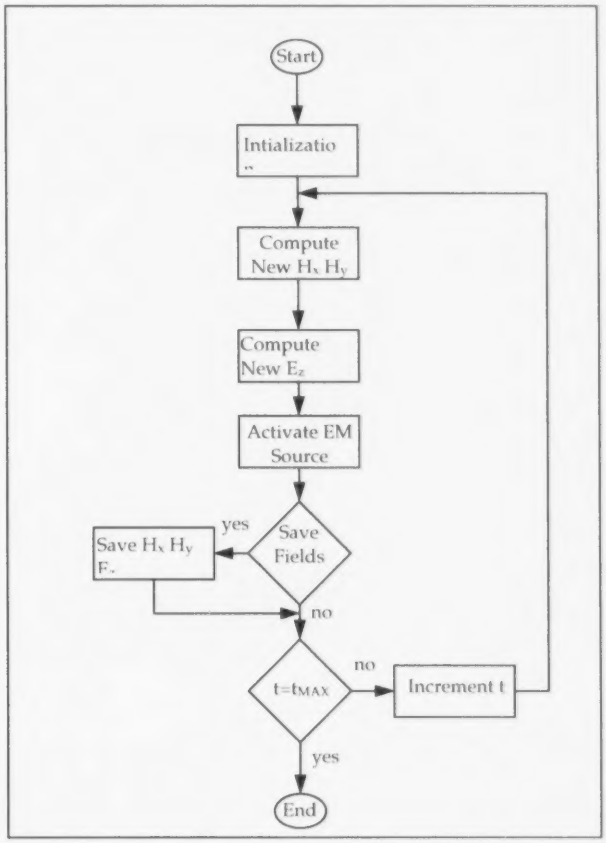

Figure 2.10 Flowchart for FDTD program.

Using the FDTD method, simulations of bends have been performed. For a ridge waveguide structure, with an index difference of 0.06, the minimum bend radius which has a loss of < 0.5 dB due to curvature is 2.0 mm.

2.2 Multimode Interference Couplers

Multimode interference couplers, or MMI couplers, are very simple but useful passive integrated components. An MMI coupler consists of a single mode input guide(s), a section of multimode waveguide and single mode output waveguides.

The location of the input guide or, in a particular case, multiple guides have a great affect on the operation of the MMI coupler, and will be discussed in detail in Section 2.2.3. The light from the input guide(s) stimulates the modes that are supported inside the multimode waveguide section. There can be as few as three or as many as 15, or more. The multimode waveguide will periodically re-focus the light along the direction of propagation back to the same lateral position as the input guide(s). Furthermore, at certain lengths a single mirror image of the input will be formed or at another length the image will be split into two equal intensity beams. By suitably position the output guides, a device that acts as a cross coupler or 3 dB splitter can be designed.

2.2.1 Self-Imaging Theory

Self-imaging refers to a property of multimode waveguides which forms an image, or multiple images, of the input field at a periodic distance in the direction of propagation [22]. Since channel waveguides of interest are single moded in the vertical direction, a two dimensional slab analysis will

suffice. Further, it can be shown that there is no loss of generality by imposing this assumption.

The analysis begins by assuming that the waveguide is strongly guiding, i.e. the exponential tails of the fields decay very rapidly in the cladding. The electric field for mode v is then given by 2.12 [23].

$$\Phi_v(x) = \sin(k_{x,v}x) \tag{2.12}$$

where,

$$k_{x,v} = \frac{\pi(v+1)}{W_{eff}}$$
$$W_{eff} \approx W + \left(\frac{N_c}{N_f}\right)^{2\alpha} \frac{\lambda_o}{\pi\sqrt{N_f^2 - N_c^2}} \tag{2.13}$$

W_{eff} is the effective width of the waveguide which takes into account of the fields penetrating into the cladding layer,

W is the nominal width of the waveguide,

N_f is the effective index of the film or core layer,

N_c is the effective index of the cladding layer,

$k_{x,v}$ is the lateral wavenumber,

λ_o is the free space wavelength,

α=0 for TE modes and α=1 for TM modes, and

v=0..N represents the mode number where a total of N+1 modes exist.

The dispersion relation, which relates the lateral wavenumber $k_{x,v}$, to the propagation constant β_v and the core effective index N_f is given by:

$$k_{x,v}^2 + \beta_v^2 = k_o^2 N_f^2 \tag{2.14}$$

where k_o is the free space wavenumber.

$$k_o = \frac{2\pi}{\lambda_o} \tag{2.15}$$

Solving for the propagation constant in the dispersion equation and using a binomial expansion yields:

$$\beta_v \approx \beta_0 - \frac{(v+1)^2 \pi \lambda_o}{4 N_f W_{eff}^2} = \beta_0 - \frac{v(v+2)\pi}{3L_\pi} \tag{2.16}$$

Notice that the propagation constant depends quadratically on the mode number, v. Therefore, there exists a definite phase relationship between each of the propagating modes. The beat length, L_π, is the length over which two modes must propagate so that they are completely out of phase with one another, i.e. a phase difference of $n\pi$. The beat length for a multimode coupler then follows as,

$$L_\pi = \frac{\pi}{\Delta\beta} = \frac{\pi}{\beta_0 - \beta_1} \approx \frac{4 N_f W_{eff}^2}{3\lambda_o} \tag{2.17}$$

2.2.2 Modal Propagation Analysis

The propagating modal analysis method (PMA) is an analytic method

used to determine the field inside a MMI device at any distance z. The input electric field from a single mode waveguide, $\Psi(x)$, at z=0 is given by

$$\Psi(x,z=0)=\begin{cases} A_s e^{\gamma_s(x+a)} & x<-a \\ A_f \cos(\kappa_f x+\phi_s) & -a<x<a \\ A_s e^{-\gamma_s(x-a)} & x>a \end{cases} \tag{2.18}$$

With the input excitation fully described by $\Psi(x,0)$, the power coupled to each mode v, can be determined. The coupling coefficients, c_v, are calculated by using the overlap integral as defined by (2.19), where it has been assumed that both $\Psi(x)$ and $\Phi(x)$ have been power normalized according to (2.8). Figure 2.11 shows the five modes represented by $\Phi_v(x)$ that exist inside the multimode coupler calculated by 2.12.

$$c_v=\int_{-\infty}^{+\infty}\Psi(x,0)\cdot\Phi_v(x)\,dx \tag{2.19}$$

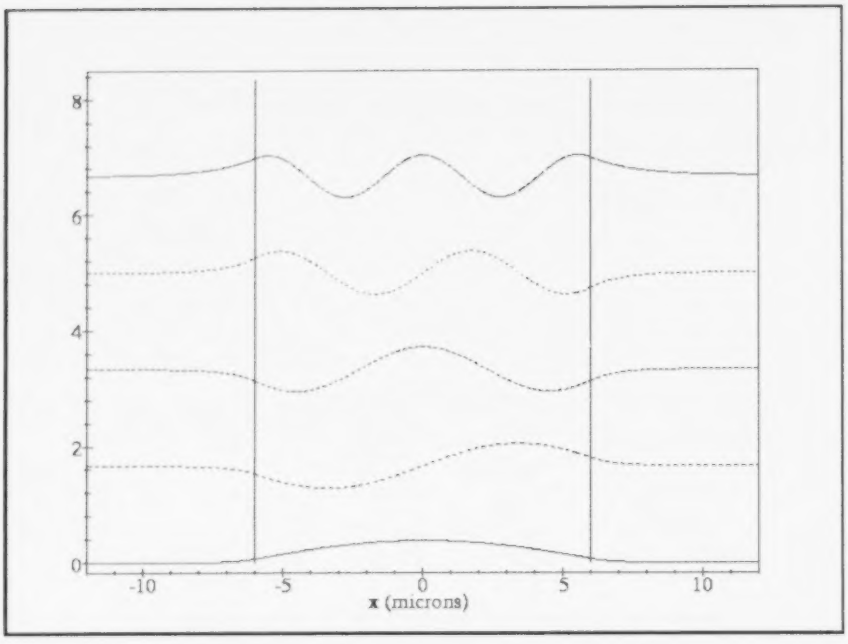

Figure 2.11 Field distribution as described by Φ_v in a MMI 12 μm wide (mode 0 through 4).

The field inside the MMI device as a function of z is now given by:

$$\Phi(x,z) = \sum_{v=0}^{N-1} c_v \Phi_v(x) e^{j(\omega t - \beta_v z)} \tag{2.20}$$

In order to simplify the presentation of the following equations, the harmonic time dependence will be suppressed (i.e. the $e^{j\omega t}$ term will be omitted). Substituting (2.16) into (2.20), equation (2.21) describes the field inside the MMI as both a function of the mode number and L_π.

$$\Phi(x,z) = \sum_{v=0}^{N-1} c_v \Phi_v(x) e^{-jz\left[\beta_0 - \frac{\pi v(v+2)}{3L_\pi}\right]} \tag{2.21}$$

Figure 2.12 illustrates the shape of the electric field distribution in the x-direction at various lengths along the MMI as calculated by the PMA method. From (2.21), it can be seen that once a waveguide dimensions and index have been chosen, the only remaining free parameter is c_v. In the next section it will be shown that c_v has a dramatic effect on image formation in the MMI.

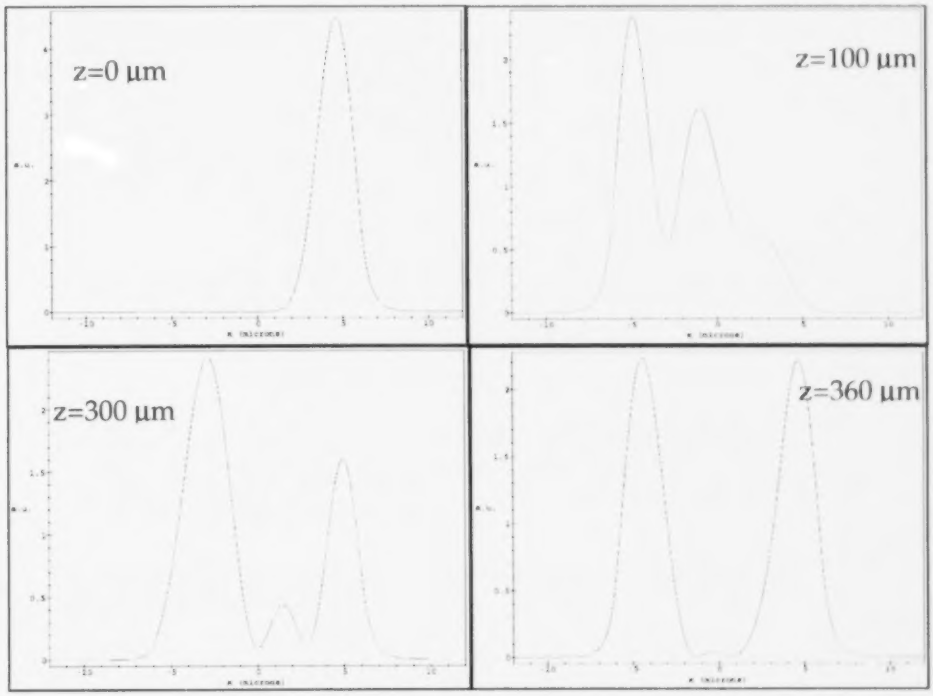

Figure 2.12 Shape of the electric field distribution in the x-direction along the length of the MMI as calculated by the PMA.

2.2.3 Effect of the Location of the Excitation Field on Image Formation: General, Paired and Symmetric Interference

Thus far, no restrictions on the lateral location of the input excitation field, $\Psi(x)$, have been imposed (see figure 2.13). If the input guide, which controls the location of the excitation field, is positioned at an arbitrary location, then the MMI device will operate under a condition termed "general interference".

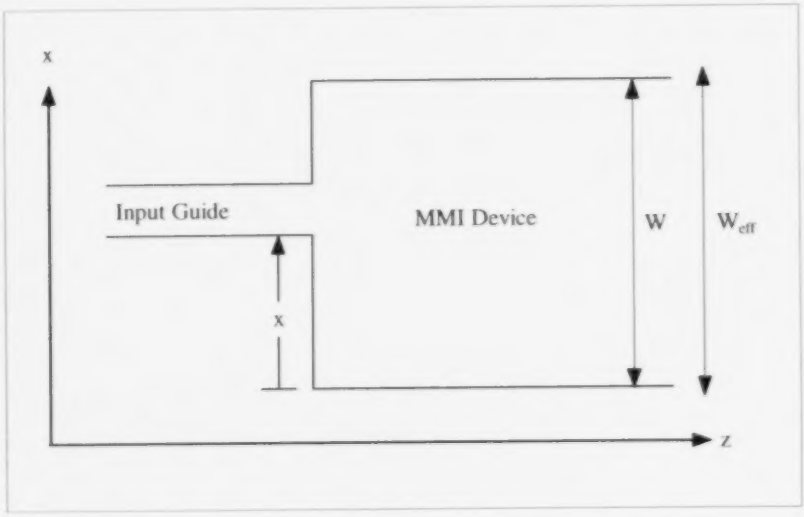

Figure 2.13 Lateral location of input waveguide for General Interference.

If on the other hand, the input guide is located at $\frac{\pm W_{eff}}{6}$, then certain coupling coefficients, c_v, will equal zero, resulting in another type of interference called paired interference (see Figure 2.14). Finally, when the MMI is centre fed by the input guide, all c_v where v is odd, will equal zero (see Figure 2.15). This type of restricted resonance results in symmetric interference.

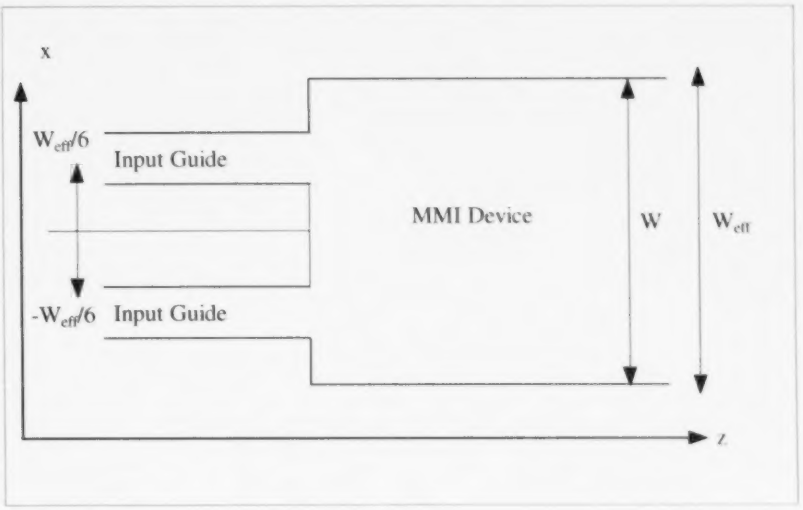

Figure 2.14 Location of input guide for Paired Interference.

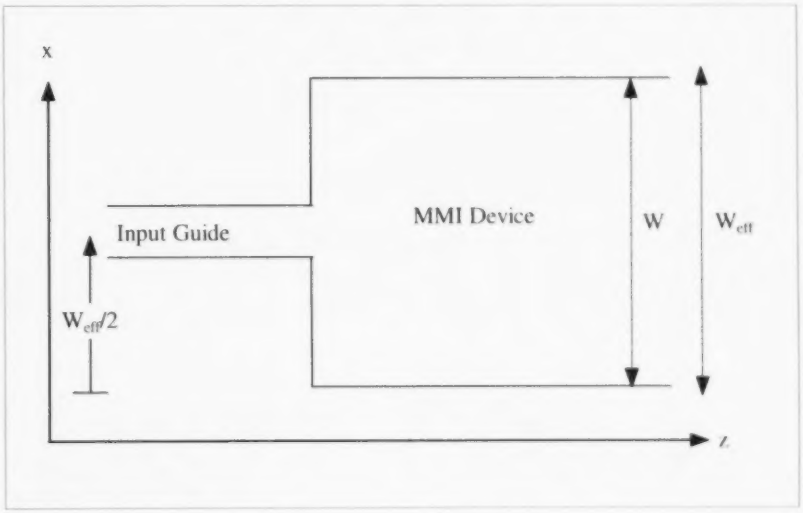

Figure 2.15 Location of input guide for Symmetric Interference.

To see how imaging occurs in MMI devices, the general interference case will be presented.

The coupler length is defined as :

$$L_{s,p} = \frac{s}{p} 3L_{\pi} \tag{2.22}$$

where s and p are integers. The electric field at $z=L_{s,p}$ is then given by

$$\Phi(x, L_{s,p}) = \sum_{v=0}^{N-1} c_v \Phi_v(x) \exp\left(j \cdot L_{s,p} \left[\frac{\pi v(v+2)}{3L_{\pi}} - \beta_0 \right] \right)$$

or (2.23)

$$\Phi(x, L_{s,p}) = A \sum_{v=0}^{N-1} c_v \Phi_v(x) \exp\left(j \cdot L_{s,p} \frac{\pi v(v+2)}{3L_{\pi}} \right)$$

where

$$A = e^{-j\beta_0 L_{s,p}}$$

Substituting (2.12) into the above equation, gives

$$\Phi(x, L_{s,p}) = A \sum_{v=0}^{N-1} c_v \sin\left(\frac{\pi(v+1)x}{W_{eff}} \right) \exp\left(j \cdot L_{s,p} \frac{\pi v(v+2)}{3L_{\pi}} \right) \tag{2.24}$$

Using the result derived in Appendix I gives:

$$\Phi(x, L_{1,1}) = A \sum_{v=0}^{N-1} c_v \Phi(W_{eff} - x) \tag{2.25}$$

where $L_{1,1}=3L_{\pi}$. Equation (2.25) describes a field that has been mirrored about the x-axis at a distance $z=3L_{\pi}$ which has the same intensity as the input field (see Figure 2.16).

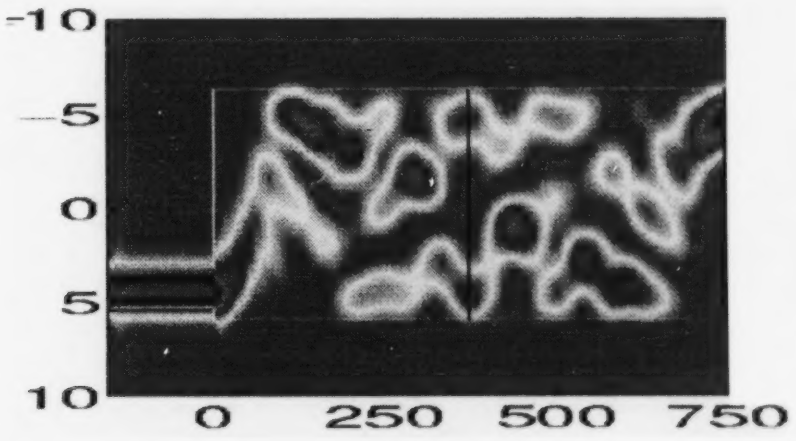

Figure 2.16 Mirror image of input field or coupler operating in the cross state (the vertical line illustrates the 3 dB length, z≅360 μm).

Using the same argument as above, with $L_{s,p}=L_{1,2}$ a pair of images, $\Phi(x)/\sqrt{2}$ and $\Phi(W_{eff}-x)/\sqrt{2}$, are formed (i.e. images at $x=\pm W_{eff}/2$ each having half the intensity of the input field $\Psi(x)$). When $z=L_{1,2}=\frac{3}{2}L_{\pi}$ or the 3 dB length, a 3 dB coupler is formed.

As previously stated, two restricted resonances can occur: symmetric interference and paired interference. The restricted resonances occur because a restriction is imposed on the values of c_v. For symmetric interference to occur, c_v for v=odd, must be made equal to zero. This situation will be satisfied if the MMI is centre fed. It can be shown that $c_v=0$, for v=odd with a centre fed MMI, by taking the overlap integral of the input field, $\Psi(x)$ with the odd modes in the MMI, $\Phi_v(x)$, v=odd. It is noteworthy that the 3 dB length of a centre-fed MMI is only *one-quarter* the 3 dB length of a general

interference MMI.

If (2.16) is examined, an effect termed "paired interference" will result if $\mathrm{mod}_3[v(v+2)]=0$ [24]. This implies that c_v=0, for v=2,5,8,... and will reduce the periodic image formation by a factor of 3 as compared to general interference. In this case, two (or four, six, etc.) input guides are used to excite the MMI.

Figure 2.17 compares a set of identical waveguides that exhibit general, paired and symmetric interference. Again, note that the 3 dB states are much shorter in the paired and symmetric devices. Table **2.1** summarizes the characteristics of the three of MMI devices.

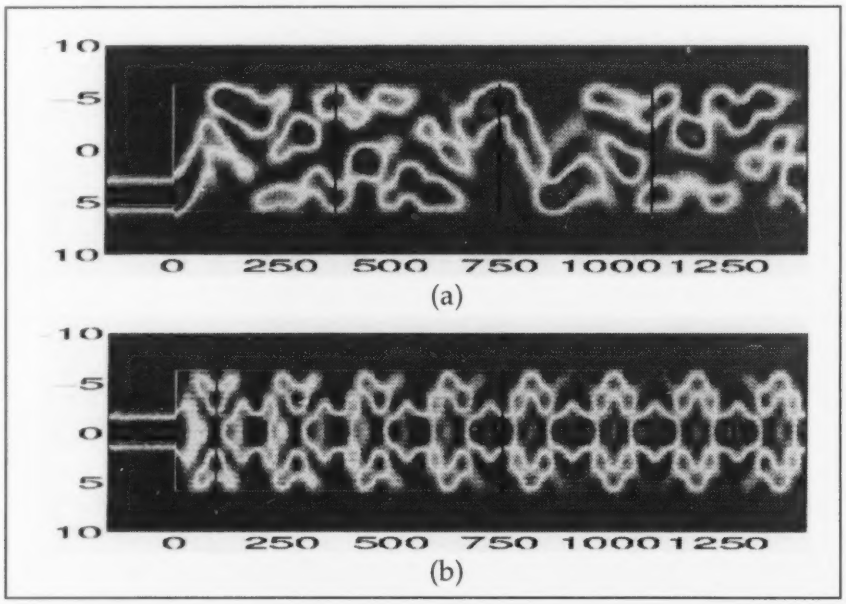

Figure 2.17 Comparison of General (a) and Symmetric (b) MMI couplers.

	3 dB state	Cross State	Bar State	Excitation and input conditions
General	$\left(m+\frac{1}{2}\right)\cdot 3L_\pi$	$(2m+1)\cdot 3L_\pi$	$2m\cdot 3L_\pi$	**none**
Paired	$\frac{m}{2}L_\pi$, **m=odd**	mL_π	$2mL_\pi$	$\mathrm{mod}_3\left[v(v+2)\right]=0$ $x=\frac{+W_{eff}}{6}$
Symmetric	$\frac{3m}{8}L_\pi$	**N/A**	$\frac{3m}{4}L_\pi$	$\mathrm{mod}_4\left[v(v+2)\right]=0$ $x=0$

Table 2.1 Summary of MMI properties.

2.2.4 Fabrication and Operational Tolerances of MMI's

There are many variables that must be optimized simultaneously in order to achieve an optimal MMI device design for a particular application. The variables can be grouped into two categories according to, fabrication tolerances and operational tolerances. Fabrication tolerances refer to how the device is affect by dimensional variations during fabrication. Operational tolerances refer to those variables that affect the performance of the device during operation, such as wavelength, temperature, and polarization.

Fabrication tolerances include variations in device dimensions,

refractive index, film uniformity, and film homogeneity. The effect of these variations on the properties of the MMI can be investigated by comparing the nominal beat length, L_π, to the beat length of a fabricated device measured experimentally. Operational tolerances can be treated in the same manner. Modal analysis can be used to investigate the performance of the device when variables such as wavelength, refractive index, etc. are varied. A closed form solution which estimates the tolerances of key variables is beneficial.

An analytical method which can predict the effect of tolerances begins by considering a Gaussian beam focused at a self-image distance L. It has been shown that the length range encompassing a 0.5 dB variation centered around a focal spot is given by the Rayleigh range [25]:

$$\delta L = \frac{\pi N_f \omega_o^2}{4\lambda_o} \tag{2.26}$$

where ω_o is the Gaussian beam waist, or equivalently the 1/e point of the field amplitude. Differentiation of (2.17) and then normalization by the length leads to

$$\frac{\delta L}{L} = \frac{\delta N_f}{N_f} = 2\frac{\delta W_{eff}}{W_{eff}} = \frac{|\delta\lambda_o|}{\lambda_o} \tag{2.27}$$

Using the above relationship together with (2.26), an estimate of the tolerances for the width, index and wavelength can be made. It is important to understand which variables have the greatest effect and the tightest tolerances on the performance of the MMI device. The tolerance of the

effective width is most difficult to achieve because the tolerance in photolithography is approximately 0.1 μm. Using (2.26) and (2.27) the tolerance of the effective width is $\delta W_{eff} \approx 0.19$ μm, which is comparable to the tolerance of the photolithography process.

2.2.5 Numerical Modeling of the Multimode Interference Couplers

Although modal propagation analysis is a useful semi-analytical method for investigating the performance of MMI couplers, the method does not take into account material dispersion, waveguide losses or material losses. Furthermore, it assumes that the modes are completely orthogonal with no coupling occurring between the modes in the MMI. To overcome these deficiencies, a beam propagation method (BPM) software program was used to simulate the performance of the MMI's couplers. Since the device has only one vertical mode, the fundamental mode, a 2-D BPM can be used with little loss of information.

A brief outline of how the BPM program works is presented. There are many types of BPM programs, using finite differencing, finite elements, eigenmodes, or others [26-28]. The BPM that was used in this work is known as a split-step BPM, since it solves the scalar Helmholtz equation in two half-steps rather than a single step. By breaking the problem into two simpler steps, the solution method becomes less difficult. Qualitatively, the first step is a refraction step and the second step is a diffraction step. The refraction

step multiplies the input field by a set of phase factors that represent the field propagating through a lens (see Figure 2.18).

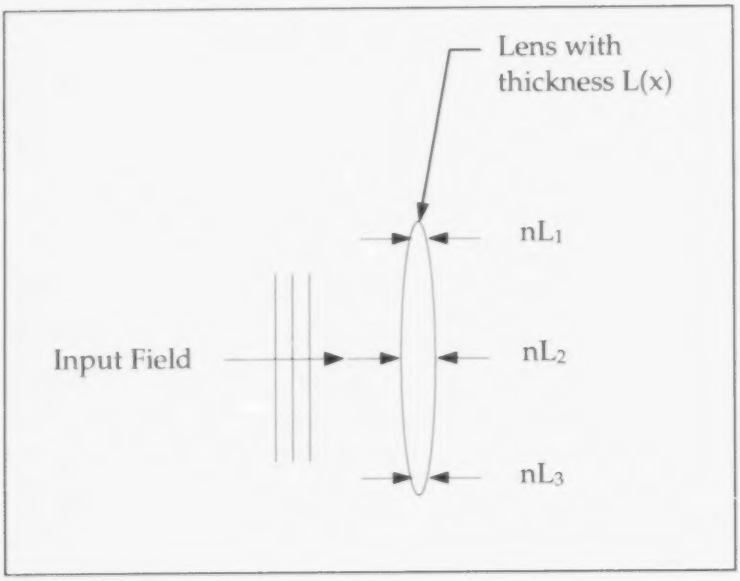

Figure 2.18 Refraction step of a BPM is equivalent to propagating the field through a lens.

The diffraction step makes use of Fourier optics. First, the fast Fourier transform (FFT) of the field derived from the first step is taken. This decomposes the field into a series of plane waves, each traveling with a different wavevector in frequency space (or plane waves with different propagation angles in real space). Subsequently, another set of phase factors is multiplied by these plane waves in frequency space to account for diffraction. Finally, the inverse FFT is then taken to reconstruct the field in real space. Results of the BPM simulations are shown in Figures 2.16, 2.17,

and 2.19. The figures obtained from the BPM simulations clearly illustrate that the input field is periodically imaged along the length of a multimode interference device.

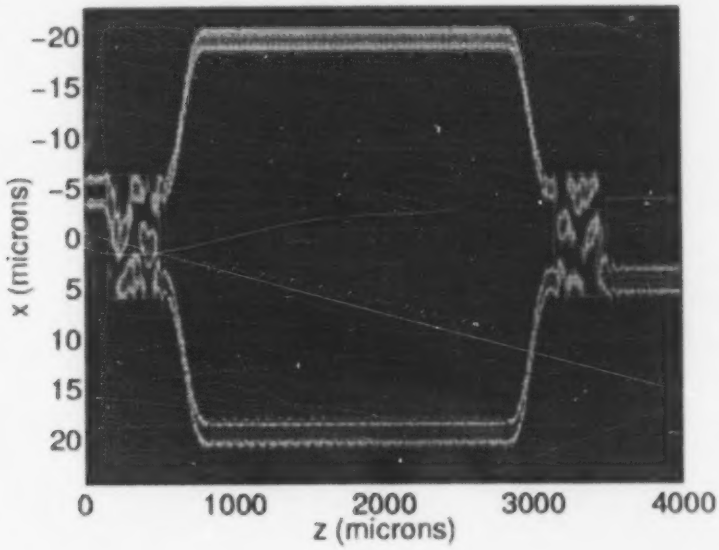

Figure 2.19 BPM simulation of the entire sensor.

2.3 Mach-Zehnder Interferometers

Interferometers are optical devices which divide a coherent optical signal into two beams: the reference beam and the delayed beam. The two beams, often traveling along different paths, are combined with one another. When the beams combine they interfere with each other producing an intensity modulated signal. There are numerous types of interferometers, such as the Mach-Zehnder, Michelson and Fabry-Perot (see Figure 2.20). Interferometers can be made as free space bulk devices or as integrated

optical devices. The Mach-Zehnder (MZ) was chosen since it does not require metallized cleaved facets to act as mirrors, resulting in a simpler device to fabricate.

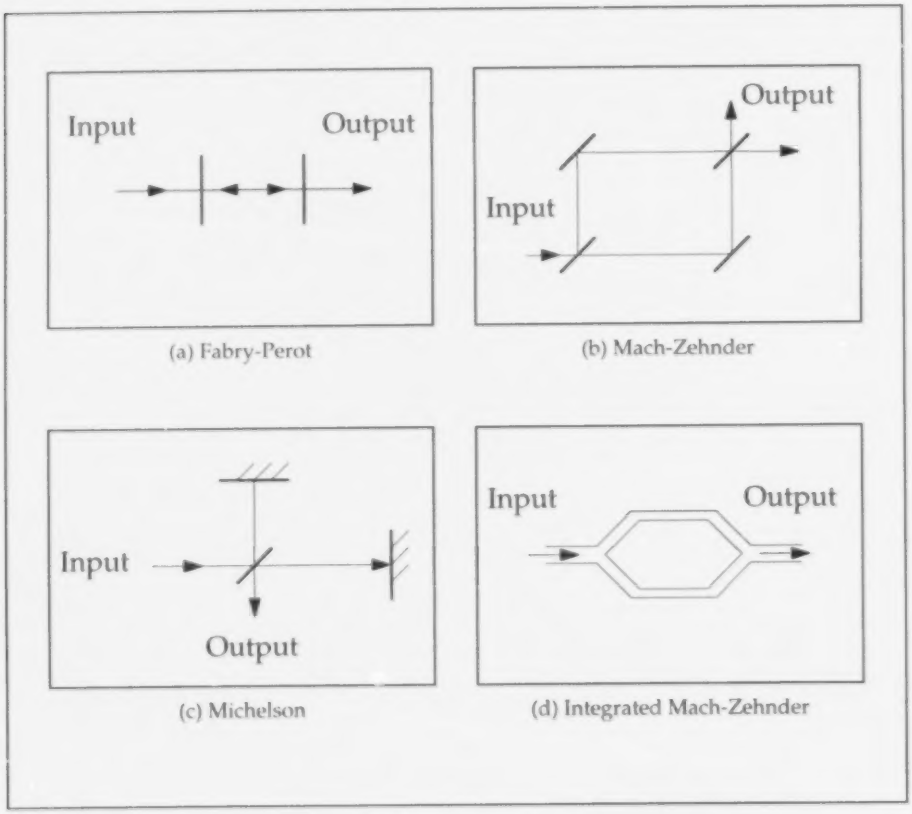

Figure 2.20 Some common types of interferometers.

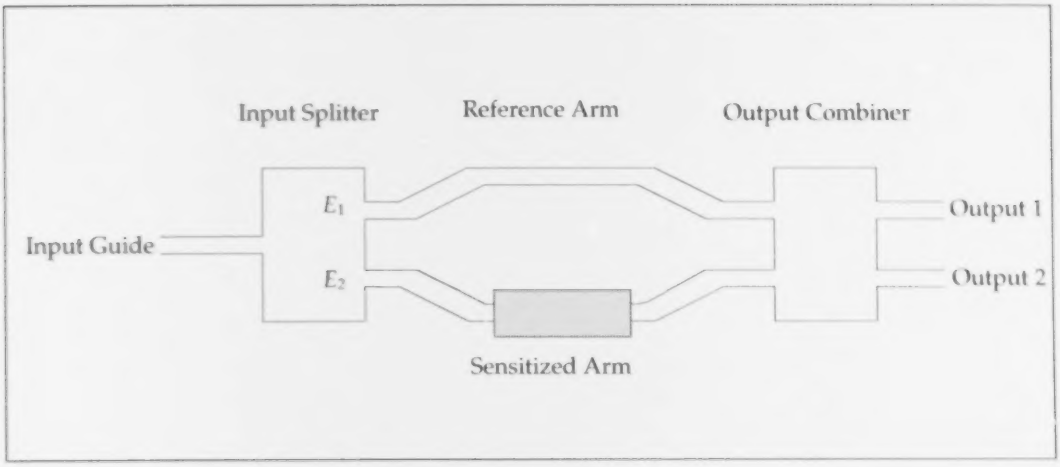

Figure 2.21 Conceptual drawing of an integrated Mach-Zehnder interferometer.

If an input field has a peak value of E_o, then the fields at Output 1 before they interfere are given by [29]:

$$E_1 = E_o\sqrt{\alpha_1 k_{I1} k_{O1}}\cos(\omega_o t + \phi_1)$$
$$E_2 = E_o\sqrt{\alpha_2 k_{I2} k_{O2}}\cos(\omega_o t + \phi_2) \qquad (2.28)$$

where ω_o is the optical frequency, ϕ is the phase, α_x is the attenuation is each arm and k_{Ix} and k_{Ox} are the tap ratios for the input and output couplers. The intensity of the two coherent signals which interfere at the output of the MZ is:

$$I = \langle E_1 + E_2 \rangle^2 = \langle E_1^2 \rangle + \langle E_2^2 \rangle + \langle E_1 E_2 \rangle \qquad (2.29)$$

where $\langle\ \rangle$ denotes the expected or time average value. Substituting (2.28) into (2.29) results in:

$$I_1 = E_o^2\left\{\alpha_1 k_{I1} k_{O1} + \alpha_2 k_{I2} k_{O2} + 2\sqrt{\alpha_1\alpha_2 k_{I1} k_{I2} k_{O1} k_{O2}}\cos(\phi_1 - \phi_2)\right\} \quad (2.30)$$

$$I_2 = E_o^2\left\{\alpha_1 k_{I1} k_{O2} + \alpha_2 k_{I2} k_{O1} + 2\sqrt{\alpha_1\alpha_2 k_{I1} k_{I2} k_{O1} k_{O2}}\cos(\phi_2 - \phi_1)\right\} \quad (2.31)$$

where I_1 and I_2 are the intensities at Outputs 1 and 2. As can be seen from the above equations, the intensity depends strongly on the phase difference. A useful figure of merit for MZ is the fringe visibility, $\mathcal{V}$, and is given by:

$$\mathcal{V} = \frac{I_{max} - I_{min}}{I_{max} + I_{min}} \quad (2.32)$$

Since I_1 and I_2 are not identical, the fringe visibility at outputs 1 and 2 will not be the same, unless the split ratio for one coupler is 0.5. This is a crucial point to note, because the fringe visibility has a direct bearing on the dynamic range of the sensor. Therefore, when designing and fabricating the couplers for the MZ, which in this case are MMI devices, the tap ratios must be close to being identical as possible.

The phase of an optical signal is defined as:

$$\phi = n k_o L = \frac{2n\pi L}{\lambda_o} \quad (2.33)$$

where n is the refractive index and L is the path length. Therefore, to induce a change in the phase, the refractive index or path length must be modulated. The path length can be changed by the application of heat with the refractive index changing as a function of temperature. The refractive index and path length will vary with temperature according to the following equations:

$$n = n_o(1+\eta T) \tag{2.34}$$

$$L = L_o(1+CTE \cdot T) \tag{2.35}$$

where n_o and L_o are the index of refraction and length at 25°C, η is the thermal optic coefficient having units of °C^{-1}, and *CTE* is the coefficient of thermal expansion of the material in °C^{-1}. Taking the tap ratios of the input and output couplers to be 50% and assuming that the attenuation in both arms is zero, then substituting (2.34) - (2.35) into (2.30) results in:

$$I_1 = \frac{E_o^2}{2}\left\{1+\cos(\Delta\phi)\right\} = E_o^2\cos^2\left(\frac{\Delta\phi}{2}\right) \tag{2.36}$$

where

I_1 is the intensity at output 1 of the MZ

$$\begin{aligned}\Delta\phi &= \phi_1 - \phi_2 \\ &= \frac{2\pi n_o L_o}{\lambda_o}\left[(1+\eta T_1)(1+CTE \cdot T_1) - (1+\eta T_2)(1+CTE \cdot T_2)\right] \\ &\approx \frac{2\pi n_o L_o}{\lambda_o}\Delta T(\eta + CTE)\end{aligned}$$

Figure 2.22 illustrates the response of a MZ to a temperature differential between the two arms where the *CTE* =10^{-7}, η=10^{-6}, n_o=1.52, L_o= 2 mm and λ_o=1.55 nm.

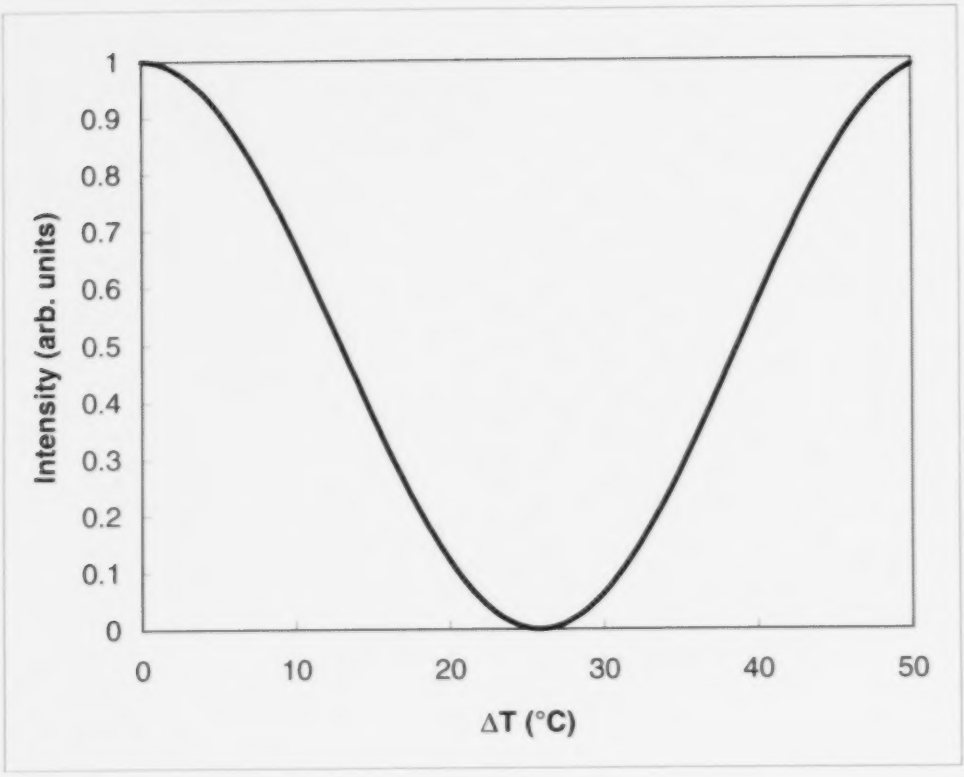

Figure 2.22 Intensity response of a MZ to a temperature differential.

In the next section, it will be shown that a microwave absorber, or susceptor, will create a temperature gradient across the MZ arms which is dependent upon microwave power. It is this temperature difference that is the transduction mechanism which converts microwave power into an optical signal.

2.4 Design and Modeling of the Susceptor

A susceptor is an object made from a material which absorbs microwave energy. Once absorbed, the energy is converted into heat. The conversion of microwaves to heat has been exploited in numerous other applications [6,7,30]. In the context of a microwave power sensor, the heat generated by the susceptor causes a temperature gradient across the MZ arms.

Since the susceptor converts microwave energy into heat, the rate of heat generation in a given microwave field partly determines the sensitivity of the sensor to microwaves. As will be shown, the dominant parameters in designing the susceptor are its size and loss factor. If the susceptor is placed inside a rectangular microwave waveguide, then a formula derived by perturbation techniques can be employed. The attenuation of a microwave field, in Neper/m, is given by [31]:

$$\alpha = 2\pi\varepsilon''_{eff}\,\frac{t\cdot h}{a\cdot b}\,\frac{\lambda_g}{\lambda_o^2}\sin\left(\frac{\pi x}{a}\right) \tag{2.37}$$

where

ε''_{eff} is the effective loss factor,

t is the width of the susceptor,

h is the length of the susceptor,

a and b are the dimensions of the microwave waveguide,

λ_g is the guide wavelength of the microwaves,

λ_o is the free space microwave wavelength, and

l is the thickness of the susceptor,

The power absorbed by the susceptor is then given by:

$$P_{abs} = 2\alpha l \tag{2.38}$$

Thus, it is the loss factor, ε''_{eff}, which determines how much microwave power is absorbed, and it is this material parameter that we seek to maximize. The effective loss factor is often divided into two parts; the loss factor, ε'', which includes dipole losses, etc. and the loss due to the electrical conductivity,

$$\varepsilon''_{eff} = \varepsilon'' + \frac{\sigma}{\omega \varepsilon_o} \tag{2.39}$$

where σ is the conductivity of the material, ω is the microwave radial frequency and ε_o is the free space permittivity. If $\frac{\sigma}{\omega \varepsilon_o} >> \varepsilon''$ then the effective loss factor is mainly dependent on the conductivity and microwave frequency.

The heat generated by the susceptor will be conducted throughout the surrounding materials according to:

$$\frac{\partial^2 T}{\partial x^2} + \frac{\partial^2 T}{\partial y^2} + \frac{\partial^2 T}{\partial z^2} + \frac{\dot{q}}{k} = \frac{1}{\alpha}\frac{\partial T}{\partial t} \tag{2.40}$$

where

α is the thermal diffusivity of the material (m^2/s)

k is the thermal conductivity of the material ($W/(m\ ^\circ C)$)

$\dot{q}$ is the heat generated by the susceptor, which is assumed to be uniform (W/m^3)

Equation (2.40) is also subject to a number of boundary conditions. For example, at the glass-air or susceptor-air boundary, a natural convection boundary condition must be applied, according to the following equation.

$$\left.\frac{\partial T}{\partial x}\right]_{x=B} = \frac{h}{k}(T - T_A) \tag{2.41}$$

where

B is the location of the boundary,

h is the heat-transfer coefficient and

T_A is the ambient temperature of the surrounding air.

If the temperature of the material is appreciable, then radiative heat transfer at the boundaries cannot be neglected, therefore, (2.41) must be modified as:

$$k\frac{\partial T}{\partial x} = h(T - T_A) + \sigma_s \varepsilon\left(T^4 - T_A^4\right) \tag{2.42}$$

where

σ_s is the Stefan-Boltzmann constant, and

ε is the emissivity of the material.

Using the above equations and a finite element software package called PDease, the steady state temperature profile was calculated. Shown in Figure 2.23 is the heat flow in the sensor and Figure 2.24 is a contour plot of the temperature that was predicted by PDease. A convective boundary condition was enforced around the perimeter of the model. The heat transfer coefficient was 0.5 and the ambient temperature was 25°C. The model indicates that a 2 °C temperature differential exists between the two MZ arms when the sensor exposed to 100 W of microwave power.

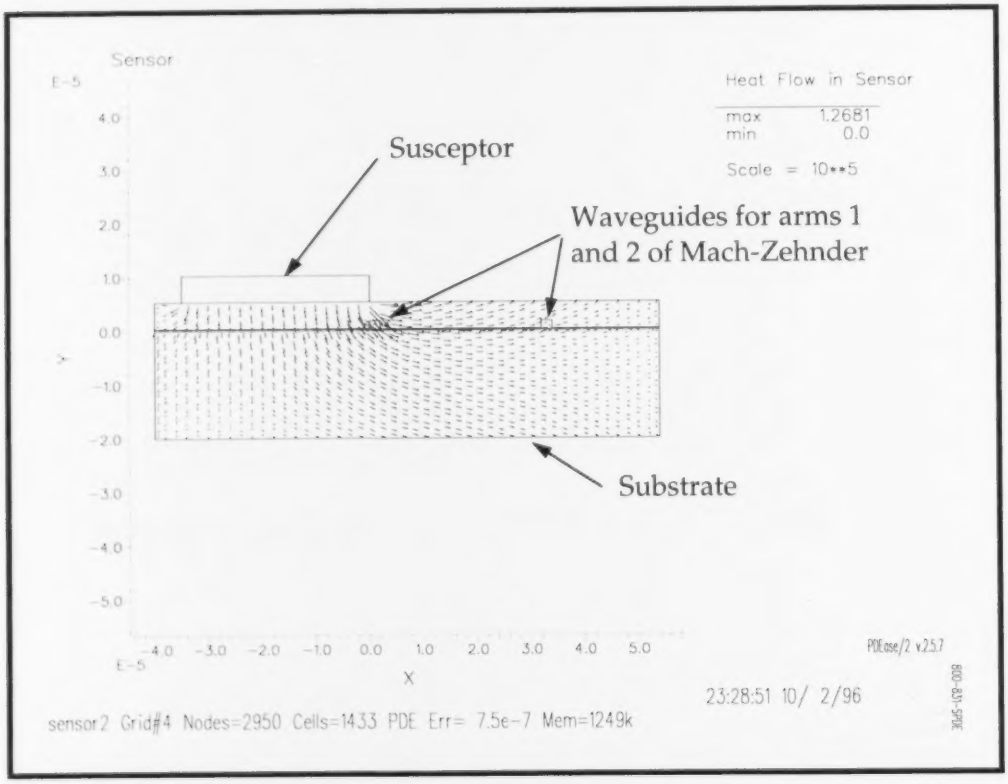

Figure 2.23 Heat flow in the sensor calculated using PDease.

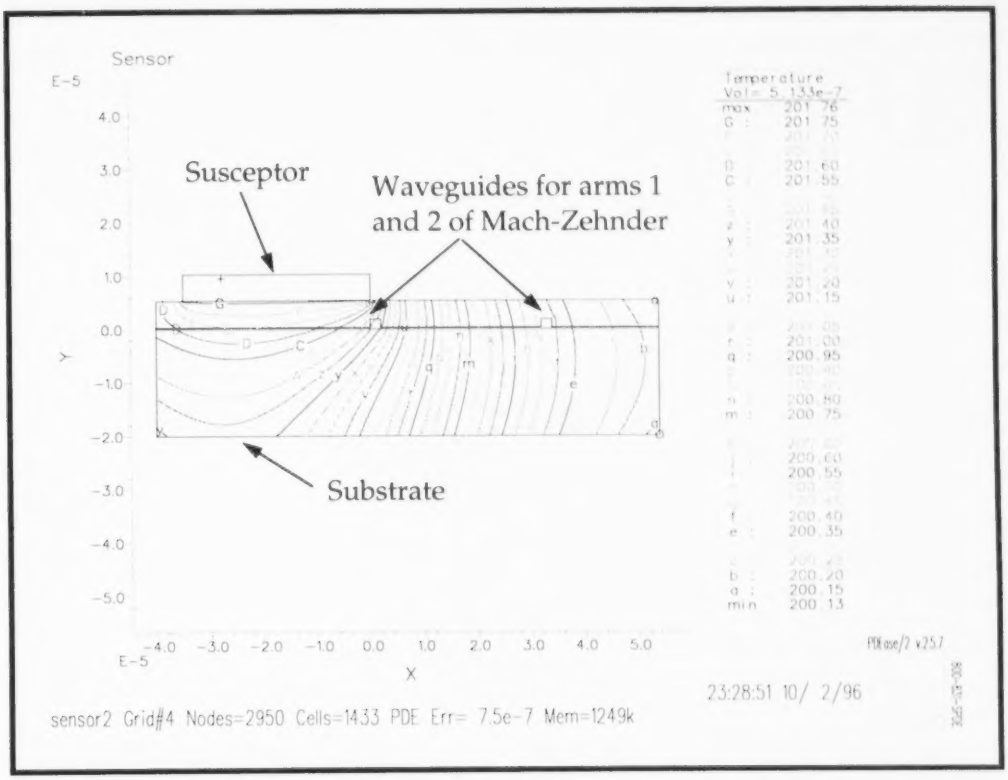

Figure 2.24 Contour plot of the temperature distribution when the susceptor is heated by 100 W of microwave power.

2.5 Conclusions

In summary, one design parameter that greatly effected the sensor was the dimensions of the single mode ridge waveguides. The width of the single mode guides dictated the minimum size and therefore the number of modes that could be supported in the MMI couplers. Increasing the width of the MMI couplers would reduce the excess loss but it would also increase its

length. Also, there was a large mismatch between the mode field diameter of the waveguides and the input fibre which results in poor coupling from the single mode fibre to the waveguide. Increasing the size of the guide would have reduced the coupling losses, however, fabrication difficulties may result.

The susceptor could not be located near the waveguide core since maintaining single mode propagation in the waveguide would require a smaller index difference between the cladding and core films, resulting in a field distribution with a slowly decaying exponential tail in the cladding layer. Since the susceptor absorbs light, it must be physically separated from the optical field, otherwise the Mach-Zehnder will have poor fringe visibility.

3. DEVELOPMENT AND EXPERIMENTS

In this chapter an overview of the sensor fabrication is presented. The procedure had two basic stages: a photolithography step and an etching step. Two prototype sensors were fabricated. Prototype I had an input guide which fed into the MMI coupler, while prototype II, had an input fibre butt coupled directly to the MMI coupler, allowing for initial testing of a symmetrical 1x2 MMI coupler. The last two sections of this chapter summarize the optical and microwave tests that were carried out on the two prototypes.

3.1 Fabrication of the Sensor

The sensor was fabricated using standard photolithography techniques using a glass-on-glass process [32]. PECVD (plasma enhanced chemical vapour deposition) was used to deposit all the films. After deposition of the films, a positive photoresist (HPR 504) was spun onto a SiO_xN_y layer. The photoresist was patterned with a chrome mask by exposure to ultraviolet light in a mask aligner. Finally, RIE (reactive ion etching) was used to etch the ridges that provided the lateral waveguiding action. The process steps used to fabricate the sensor are:

1. Deposition of a 5 μm thick lower cladding film of SiO_2, having a refractive index of 1.46, on a Corning 7059F glass substrate.

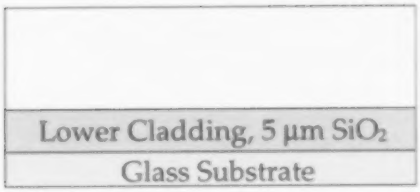

2. Deposition of SiO_xN_y waveguide core material, 1.8 μm thick, with n_f=1.52.

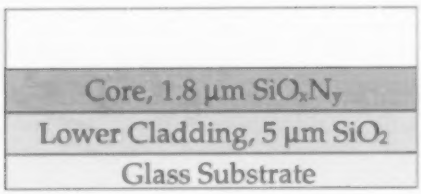

3. Spinning on positive photoresist at 4500 rpm (~1.1 μm thick).

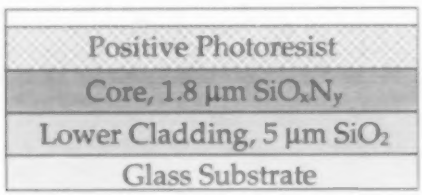

4. Exposure of resist using chrome mask in mask-aligner.

5. Hand developing of resist in a developer solution.

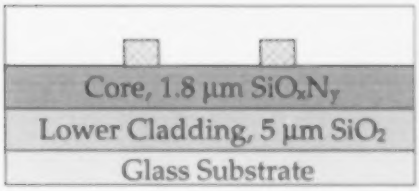

6. Etching of the core material in an RIE chamber.

7. Stripping of excess resist with an O_2 plasma and/or in acetone placed in an ultrasonic bath.

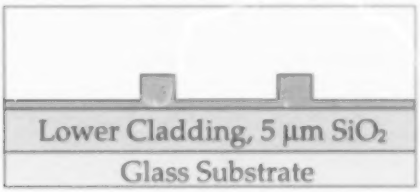

8. Deposition of a 5 µm thick upper cladding layer of SiO_2.

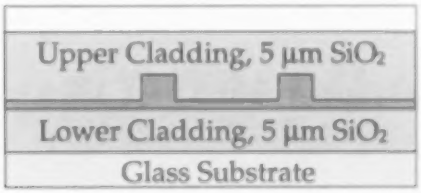

9. Dispensing of colloidal graphite through a pressurized syringe on the upper cladding layer to create the susceptor.

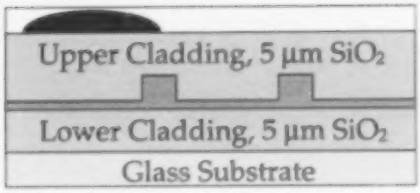

Film thickness and refractive index were verified using a prism coupler. By monitoring the thickness and index, it was possible to fabricate a device with specifications that were very close to the original design specifications. Figures 3.1 and 3.2 are SEM (scanning electron microscope) pictures of the coupler section for prototypes I and II, respectively. Note the waveguide sidewall roughness and that the waveguide walls are not precisely vertical. The sidewall roughness, as shown in Figure 3.3, resulted in higher than expected propagation loss for the single mode waveguide. A reflow step should reduce the sidewall roughness, however, the glass transition temperature of the SiO_xN_y core material was estimated to be > 1200°C and access to furnaces in this temperature range were not achievable. The sidewall roughness was reduced for the second prototype by improving the photolithography and RIE processing steps.

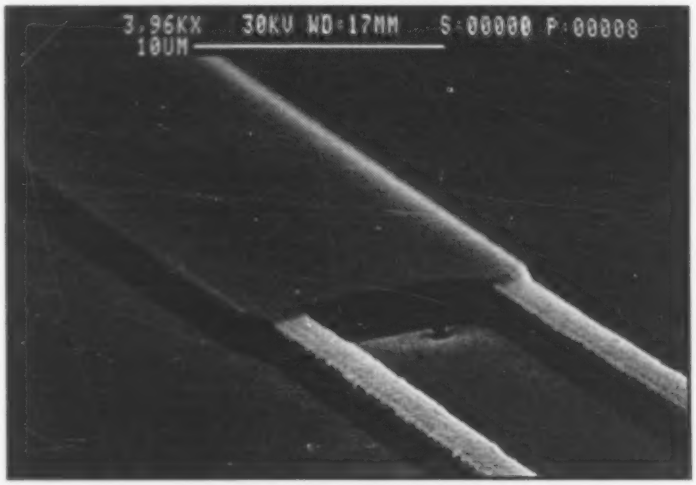

Figure 3.1 SEM picture of MMI coupler prototype I (output end).

Figure 3.2 SEM picture of MMI coupler prototype II and part of the MZ arms.

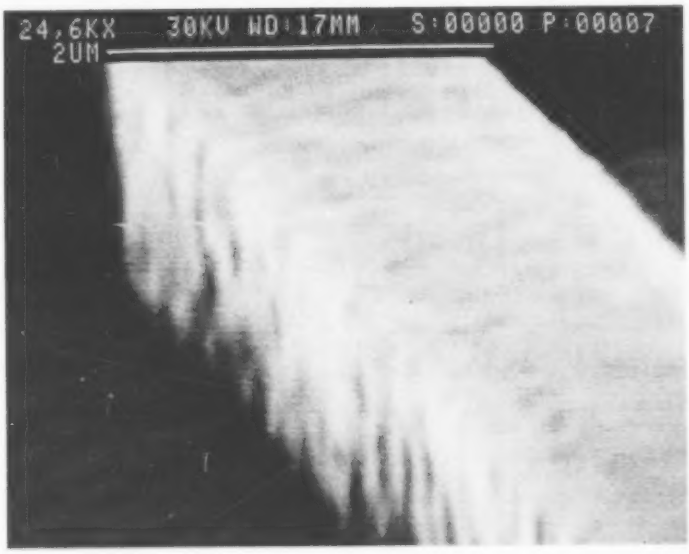

Figure 3.3 SEM picture of the sidewall roughness occurring on the waveguide sides (prototype I).

The width of the single mode waveguides was 2.0 μm ±0.1 μm and the multimode coupler sections were 11.9 μm ±0.2 μm wide as measured from the SEM. The refractive index of the core was measured to be 1.52 at a wavelength of 633 nm. The prism coupler used to measure the thickness and refractive index was only equipped with a He-Ne laser; a 1550 nm source will be attached in the near future to enable measurement at the latter wavelength. The chrome mask contained a number of permutations of the same basic sensor design. The MZ arm length was varied from 200 μm to 2 mm and the MMI coupler length was varied from 347 μm to 387 μm. The sensor which had a MMI coupler length of 367 μm and a MZ arm length of 2 mm was chosen as the optimal device because it exhibited the lowest throughput loss.

3.2 Optical Tests

Before the sensor could be tested in a microwave field, its optical performance had to be characterized. Parameters of prime importance included: coupling loss, propagation loss, MZ arm imbalance and total throughput loss. By heating the graphite susceptor with a high power laser beam, the switch/sensing performance could be mimicked. These tests were used to determine whether the device should be packaged and tested in the microwave cavity.

The setup used for optical characterization of the sensor is shown in Figure 3.4. A pigtailed 1550 nm isolated DFB (distributed feed back) laser was connected to the single mode input fibre using PC/FC connectors. Multimode 50 μm step index fibres were used to collect the light from both sensor outputs. The multimode fibres were then connected to a germanium detector head of an optical power meter. The XYZ positioners used had electrostrictive actuators which allowed ~30 μm of high precision, hands-free travel. These positioners were indispensable in aligning the input and output fibres since touching the positioning stage drastically altered the power coupled into the input waveguide. Optimal coupling was achieved by using the UV source and electrostrictive actuators which enabled hands-free alignment of the fibres to the waveguide. A drop of UV curable polymer was placed on the end of the waveguide. The electrostrive actuators were then adjusted from the control box while the output power was monitored. Once the power transfer was a maximum, a UV source was used to cure the polymer.

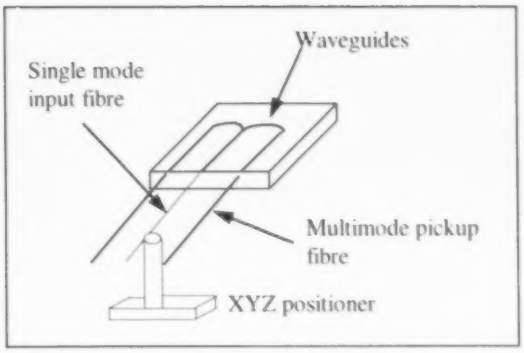

Figure 3.4 Optical test setup.

Three parameters were measured: propagation loss, MZ imbalance, and total throughput loss. For all measurements, a single mode input fibre was butt coupled to the waveguide using index matching fluid to eliminate Fresnel losses at the air/glass interfaces. The alignment of the input fibre was adjusted using electrostrictive XYZ positioners until maximum power transfer was obtained between the input and outputs.

Two methods used to determine the propagation loss were: cut-back and out-scatter. To use the cut-back method, a butt coupled fibre or lens is used to couple light into a straight waveguide. The length of the guide and throughput loss is measured and recorded. Then a section of the same waveguide is removed or cleaved off. The length and throughput loss for the shortened guide is again measured. This process is repeated until a satisfactory number of data points has been acquired or when the guide becomes too short to cleave/cut. A measurement of the waveguide loss can

be determined, since the coupling losses are approximately the same for each measurement. A slight modification of the cut-back method requires multiple waveguides having different lengths to be fabricated on the same substrate. For instance, this can be accomplished by using a series of waveguides each having a 90° bend. Again, since the coupling losses are nearly identical, the propagation loss can be determined.

The side-scattered light method involves measurement of scattered light in a lossy waveguide. Measurement of scattered light intensity can be used to determine the propagation loss. A multimode fibre is scanned along the waveguide perpendicular to the film surface or an image of the scattered light can be obtained using a CCD camera (see Figure 3.5). Once the intensity of the scattered light is plotted, the average change in scattered light versus waveguide length is a direct measurement of the propagation loss. The cut-back method could not be used because the waveguides used were too short to be cut without cracking. Therefore, the scattered light method was used to estimate the propagation losses. Calculations indicated that the propagation loss is approximately 1 dB/cm at 1550 nm.

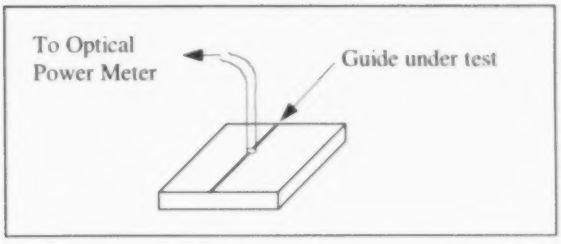

Figure 3.5 Test setup for measurement of propagation loss using the out-scatter method and a multimode fibre.

To determine the MZ imbalance or the deviation from an optimum 3 dB coupling ratio, a MZ was cut in two, as shown in Figure 3.6. The imbalance, in dB, was computed according to the following equation:

$$P_{imb} = 10\log_{10}\left(\frac{P_1}{P_2}\right) \tag{3.1}$$

where P_1 and P_2 were the output power detected by the power meters at outputs 1 and 2, respectively. For prototype II, the arm imbalance was measured to be 0.26 dB. Using the information obtained from measuring the imbalance and knowing the propagation loss, it was then possible to determine the insertion loss of the 1x2 MMI coupler. The insertion loss of the MMI coupler was calculated to be ~0.5 dB, assuming that the input and output couplers had the same loss.

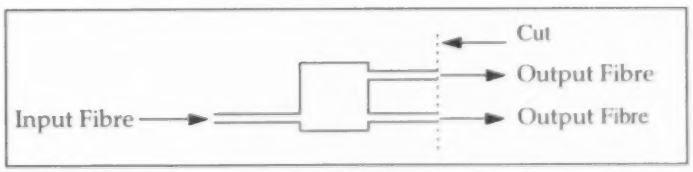

Figure 3.6 Setup for determine the imbalance of the Mach-Zehnder.

The total throughput or fibre-to-fibre loss, P_{TOT}, was calculated using:

$$P_{TOT} = 10\log_{10}\left(\frac{P_{in}}{P_1 + P_2}\right) \qquad (3.2)$$

where P_{in} was the optical power present at the input fibre, and P_1 and P_2 were the optical powers at outputs 1 and 2, respectively. The lowest fibre-to-fibre loss for prototype II was measured to be 11.9 dB.

The final optical test determined whether heat generated by the susceptor caused a sufficient index change in the nearest arm of the MZ to switch the light from output 1 to output 2. Two 5 W argon ion lasers pumped a Ti:Sapphire crystal, to produce approximately 600 mW of 980 nm light. The 980 nm light was collected using a lens and focused into a multimode fibre used to deliver the light to the susceptor. The graphite susceptor absorbed the laser light and was actually partially removed due to the high power density present, i.e. the colloidal graphite film was likely ablated off the surface. By reducing the power level to 200 mW, the susceptor remained intact and heated the surrounding material, causing the expected switching operation. The power at output 1 increased by 2.7 dB and the power decreased by 3.1 dB at output 2. The test served to verify that the switching/sensing ability of the prototype was operational.

3.3 Assembly of the Sensor

Before microwave tests could be performed, the optical fibres had to be cemented to the waveguides. Fibres which were butt coupled to the substrate edge and cemented in place can easily detach from the waveguide without proper strain relief. As a result, a larger, backing substrate was cemented to the sensor, as shown in Figure 3.7, to give the adhesive more contact area and provide a more secure bond. Extra adhesive was deposited near the edge of the backing substrate to act as a strain relief for the fibres. The final package was of adequate strength and robustness to be placed in a microwave cavity. Figure 3.8 is a picture of the assembled prototype II sensor.

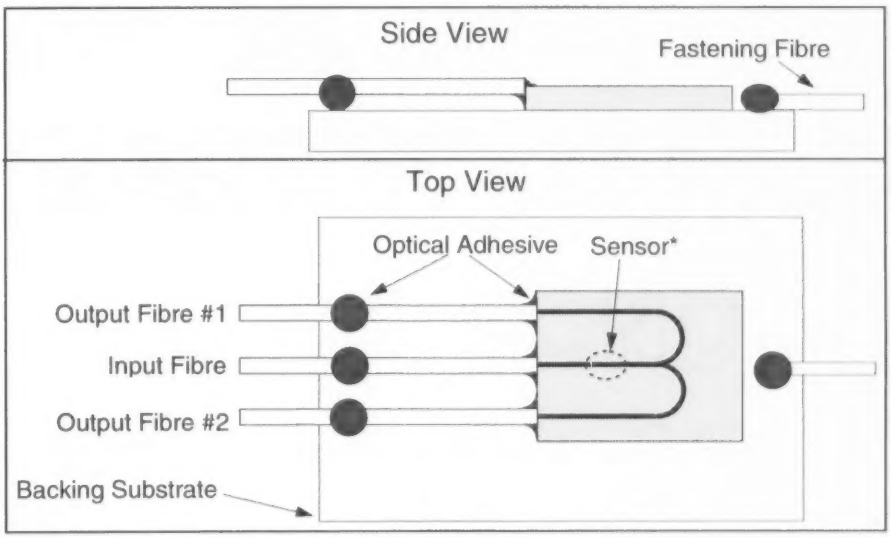

Figure 3.7 Drawing of assembled sensor. For a detailed drawing of the sensor see Figure 2.21.

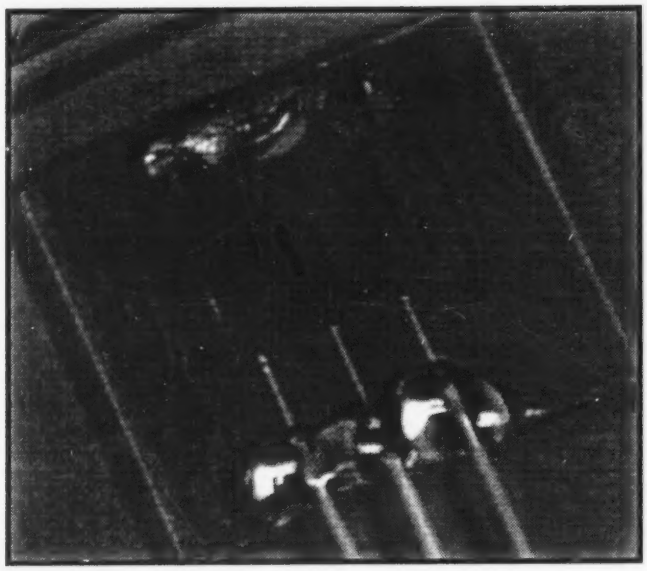

Figure 3.8 Picture of sensor prototype II.

3.4 Microwave Tests

Microwave testing of the power sensor was performed in a TE_{10} waveguide microwave applicator (a metallic structure which is used to apply microwave energy to an object, often a single mode or multimode resonant cavity). The test setup is shown in Figure 3.9 and an enlarged detail drawing of the microwave applicator is shown in Figure 3.10. WR-284 microwave waveguides (outer dimensions of 7.62 cm by 3.81 cm) were used to interconnect the microwave components .

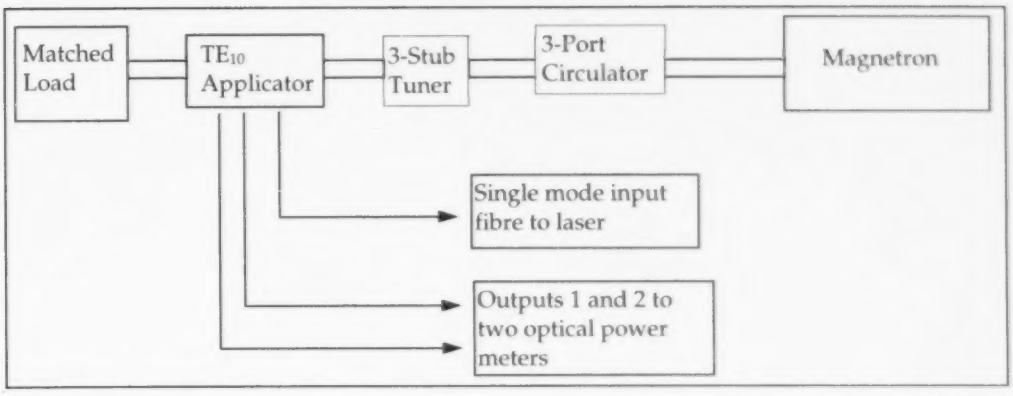

Figure 3.9 Microwave test setup.

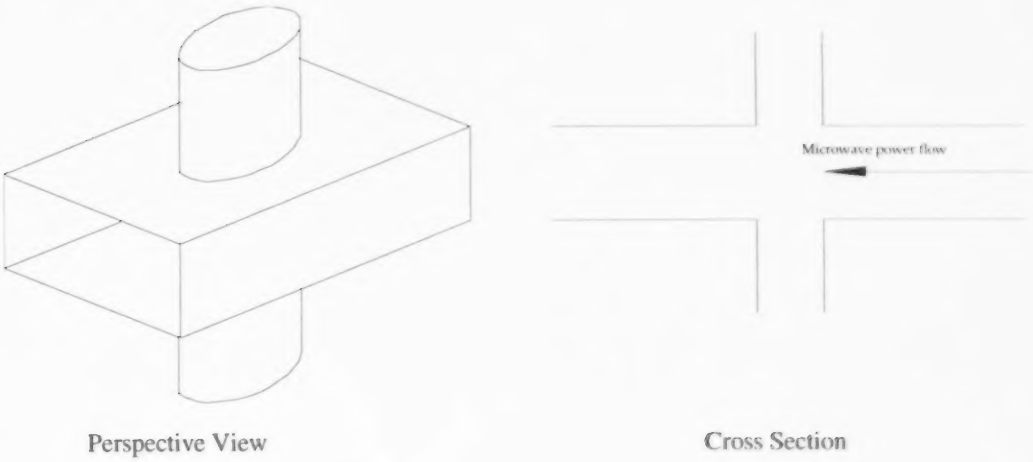

Figure 3.10 Enlarged view of the TE_{10} microwave applicator.

A magnetron capable of producing microwave power ranging from 0 to 3 kW at a frequency of 2.45 GHz, was connected to a 3-port circulator. Ports one and two were connected to the source side and load side of the microwave circuit, respectively. The third port was connected to a water cooled absorber. The circulator and absorber were used to prevented reflected

power from heating the magnetron. Next in line, was a crystal evanescent power meter attached to the broad wall of a section of waveguide used to measure reflected power. It operates by sampling the evanescent field in a microwave waveguide and rectifying the microwave electric field to obtain a signal proportional to microwave power. Following the reflected power, three posts of a 3-stub tuner were lowered and raised to match the source impedance to the load impedance, i.e. to minimize the reflected power level. The microwave waveguide applicator was next. It consisted of a standard TE_{10} waveguide which had a tube, 4 cm in diameter, passing through the broad wall of the waveguide, as shown in Figure 3.10. Since the dimensions of the tube were below the cutoff wavelength for 2.45 GHz microwaves, the sensor could be lowered into the applicator by hand without fear of exposure to microwave radiation. The sensor was held in position by taping the sensor's fastening fibre to the outside of the applicator.

At the end of the microwave circuit was a single mode cavity resonator filled with ceramic material. The ceramic absorbed the microwave power and converted the energy into heat. A water cooled absorber, similar to the one in the circulator, could also have been used in place of the ceramic load; unfortunately such an absorber was not available.

Various tests were conducted to see how sensitive the optical power sensor was to orientation with respect to microwave power flow, i.e., sensitivity to polarization. The first test was done with the sensor

perpendicular to the direction of microwave power flow. In another test, the sensor was rotated so that it was parallel to the direction of microwave power flow (see Figure 3.11).

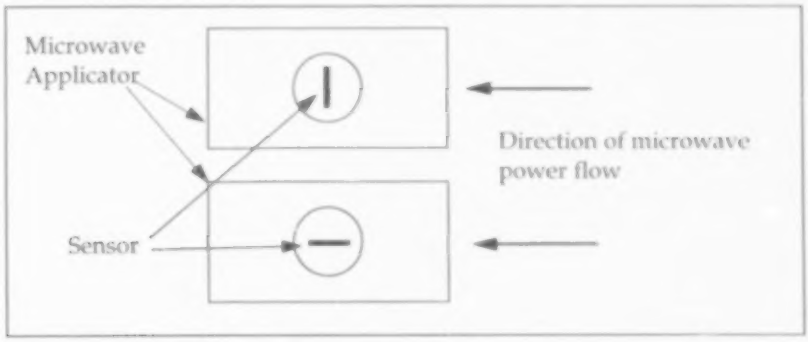

Figure 3.11 Top-view of the microwave applicator showing the two different sensor orientations tested.

Figure 3.12 shows the response of prototype II to microwave power when the sensor was positioned in the centre of the applicator and perpendicular to the microwave power flow while Figure 3.13 shows the response when the sensor was orientated parallel to the direction of microwave power flow. Figure 3.14 shows the response of prototype I to microwaves under the same testing conditions as used for prototype II with the sensor orientated perpendicular to the direction of microwave power flow.

The measurements shown in Figures 3.12 and 3.13 were performed three times. For each iteration the same response resulted, however, there was some hysteresis. Therefore, a calibration curve would consist of recording the optical power while the microwave power is increased and

then decreased. With a knowledge of the hysteresis, its impact can be reduced on measurements.

Since the microwave power was increased in a step-like fashion, the response time of the sensor could also be determined. Figure 3.15 shows a typical plot of how the sensor responded to a step change in microwave power. The response time, (time to get from 10% to 90% of its equilibrium value) was calculated to be approximately 80 seconds when the microwave power was increased by 50 W.

Both prototype sensors responded adequately to microwave power. The second prototype proved to be insensitive to the polarization of the microwave field with a sluggish response. The thermal mass of the glass substrate may be acting as a heat sink, which results in the temperature profile taking over a minute before it reaches equilibrium. Hence, future design modifications will be necessary.

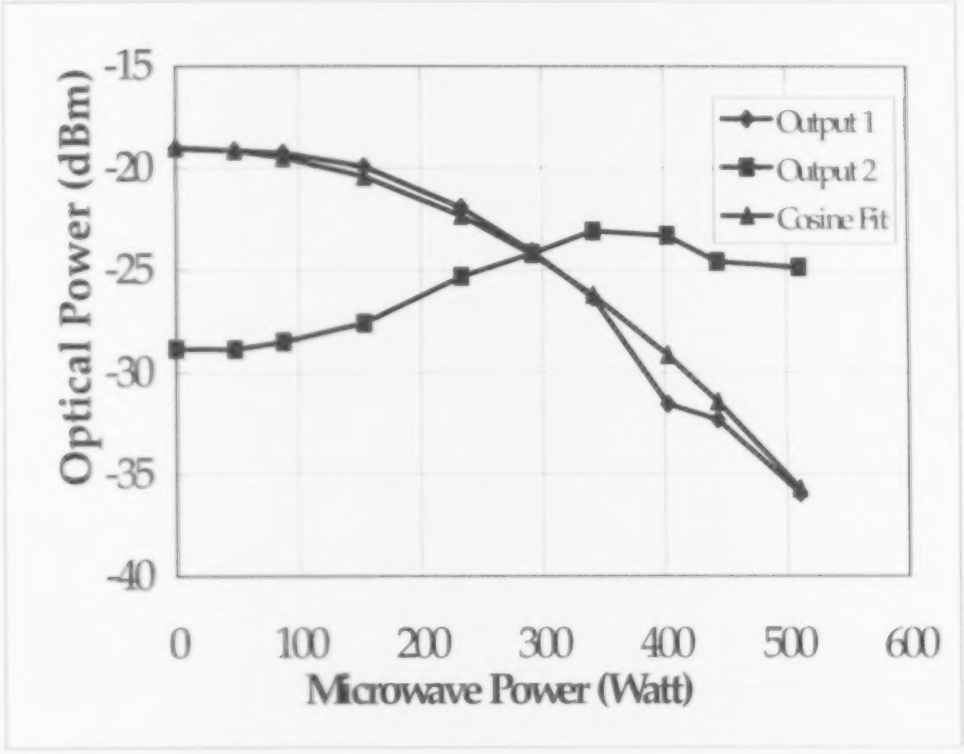

Figure 3.12 Response of sensor prototype II to microwave power when tilted perpendicular to the direction of microwave power flow. Note: The plot for output 2 was shifted up by 40 dBm.

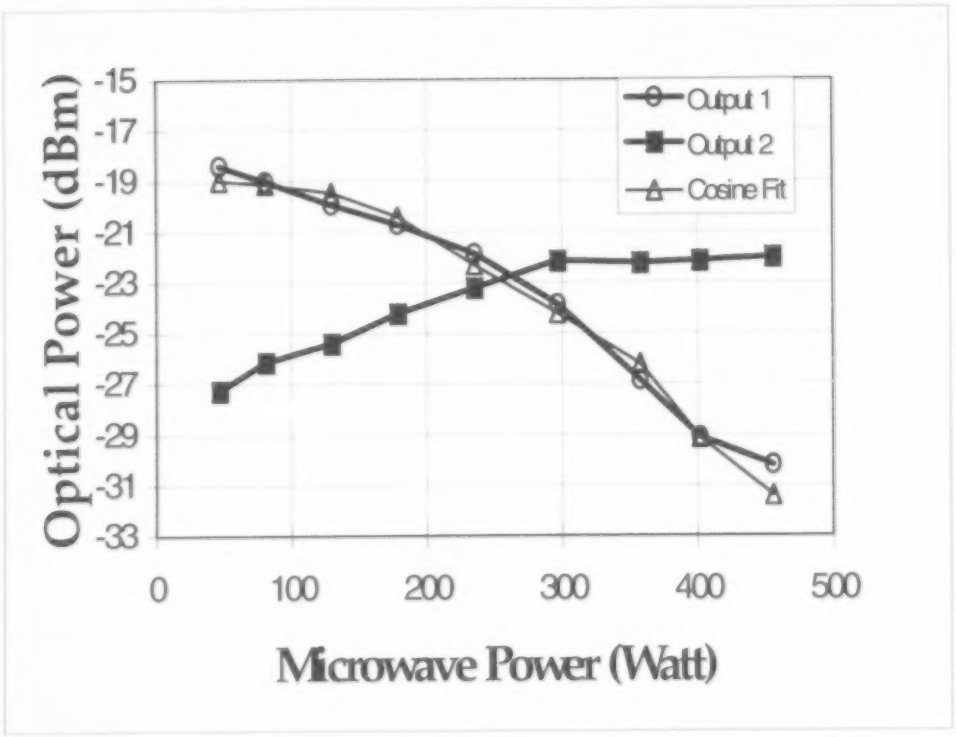

Figure 3.13 Response of prototype II to microwave power when tilted parallel to the direction of microwave power flow. Note: The plot for output 2 was shifted up by 40 dBm.

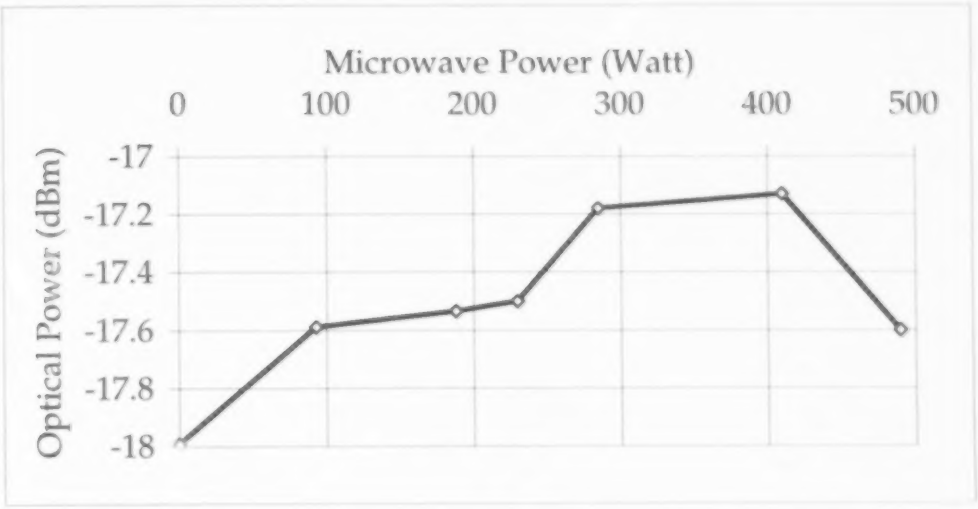

Figure 3.14 Response of sensor prototype I to microwave power (output 2 was not functional).

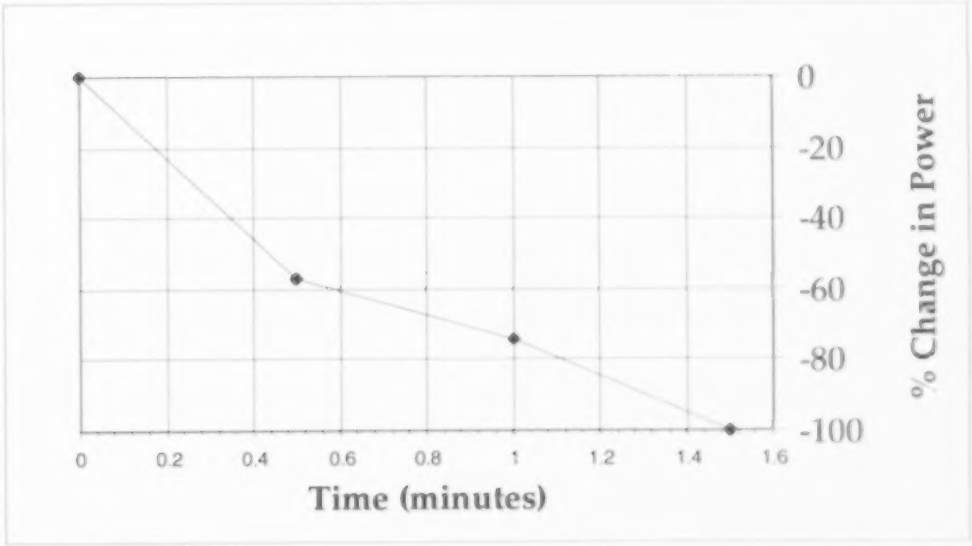

Figure 3.15 Response time of prototype II to a 50 Watt change in microwave power (power setpoint was 200 W).

4. DISCUSSION OF RESULTS AND PRACTICAL CONSIDERATIONS

In this chapter some of the difficulties encountered with both the construction and operation of the sensor will be discussed. A comparison between the modeled and experimental results will be used as a guideline in determining how good the models were at predicting experimental results and conversely their limitations. The last two sections of this chapter examines some of the potential barriers that must be overcome before a commercial product could be produced. Many areas, such as quality control, costing, etc., have not yet been addressed, but must be investigated before commercialization is feasible. Furthermore, improvements in the dynamic range, response time, size and accuracy of the sensor must still be pursued, which will be discussed in the final section.

4.1 Comparison of Modeled Results to Experiments

Three models were used in designing of the sensor: an optical model of the device, a heat transfer model, and a material and microwave interactions model. While the optical model was fairly accurate, the thermal and microwave models were more difficult to establish. These models required knowledge of parameters which are difficult. For Example without accurate knowledge of the CTE, thermal-optic coefficient, thermal conductivity,

specific heat, density and microwave loss factor for the various materials, it was very difficult to create a comprehensive model of the entire sensor. Much research is underway, for various reasons, to determine the microwave loss factor of many materials a function of both microwave frequency and temperature. Even when approximate values were chosen, the theoretically predicted performance was very different from the experimental results. By making appropriate assumptions and by adapting the models heuristically using the experience gained from each successive experiment, the models were rendered useful in formulating specific design changes. The most critical assumption made was the temperature gradient caused by the susceptor only heated the nearest arm of the MZ and created a uniform index change along the length of that arm.

Although it is difficult to compare the modeled and experimental results directly, some interesting comparisons can still be made. Assuming the thermal-optic coefficient, $\eta \approx 5 \times 10^{-6}\ ^{\circ}C^{-1}$, and $CTE \approx 5 \times 10^{-7}\ ^{\circ}C^{-1}$, the temperature difference between the two arms as a function of microwave power could be determined as shown in Figure 4.1. A maximum temperature difference of approximately 40 °C was obtained when 450 W of microwave power was present.

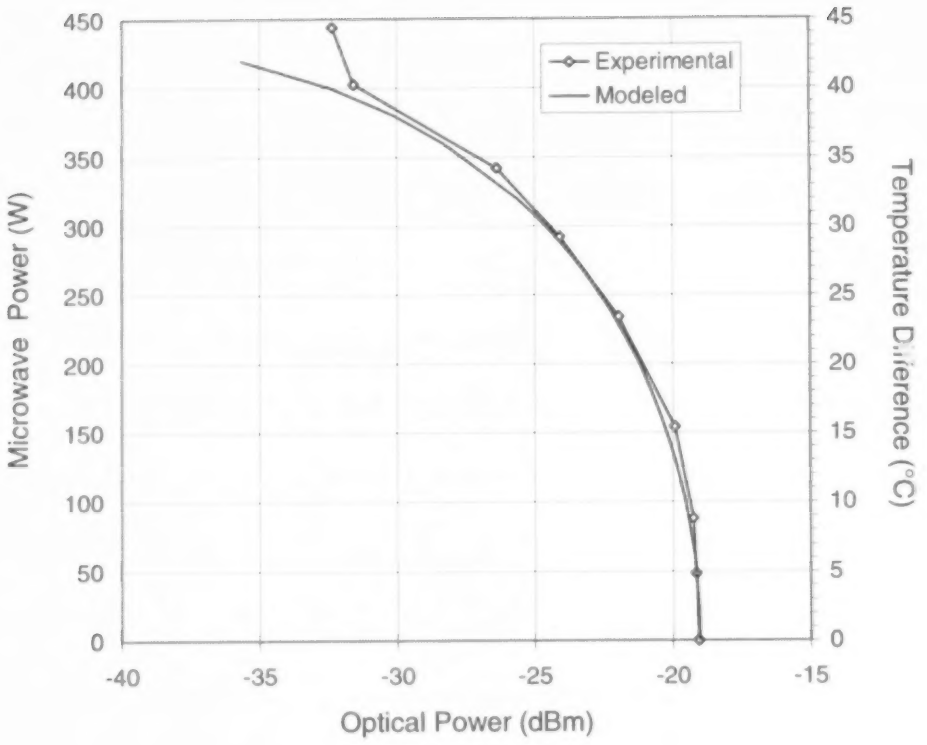

Figure 4.1 Comparison between modeled and experimental results using the MZ transfer function equation.

The modeled optical performance indicates that the input coupling loss was ~ 8.8 dB and that the insertion loss was ~ 0.5 dB per coupler. Therefore, the modeled total throughput loss is 9.8 dB for the sensor. When the fibres were butt coupled to the sensor and index matching fluid was used, a throughput loss of 11.9 dB was obtained. The difference between these two values is attributed mainly to the propagation loss caused by scattering centres and material absorption, and higher than expected insertion loss for

each MMI coupler. There is a general consensus that glass waveguides with propagation losses of < 0.1 dB/cm can be obtained. As can be seen from Figure 4.1, the total throughput loss of the device is 19 dB. The 7.1 dB discrepancy between experiment and theory resulted from the butt coupling of the fibres. Initially, the fibres were aligned with the waveguide and produced the expected 11.9 dB of loss, however, as the adhesive cured the fibres moved slightly, increasing the input coupling loss. The alignment of the input fibre to the sensor waveguide is very dependent on horizontal, vertical and angular offsets. For example, if the input fibre was horizontally offset by 2 μm, a loss penalty of ~ 1.2 dB would be incurred. Therefore, it is crucial that the fibre-to-waveguide alignment be accurate and robust.

4.2 Difficulties Encountered with Sensor Prototypes I and II

Although the sensor adequately responded to microwave power, some shortcomings were observed. First, as mentioned previously, the fibres moved out of alignment when the optical adhesive was cured. Second, when the susceptor generated heat, the temperature caused the optical adhesive to expand, which resulted in a fibre-to-waveguide coupling factor that was dynamically changing as a function of temperature. It was apparent from data taken with one version of the first prototype that two beam interference was not causing the signal variation. The intensity variation was likely due to the movement of the fibre-waveguide bond. Last, the scattering centres

and waveguide sidewall roughness resulted in excessive propagation loss.

The first two problems arise from using optical adhesive to cement the fibres to the sensor. The single mode input fibre was much more susceptible to misalignments because its mode field diameter at 1550 nm is approximately 10 μm (the core diameter is approximately 9 μm). The two multimode output fibres have a larger core diameter and are therefore much less sensitive to misalignment. Other methods of cementing the fibers must be investigated, otherwise the device will be much too difficult to calibrate and use.

The last problems were due to fabrication difficulties. The films had volume defects which scattered the light out of the waveguide and rough sidewalls, resulting in excessive propagation loss. The defects could be easily seen with the aid of a optical microscope. The effects of the defects could be lessened by annealing the films above their glass transition temperature. Ideally, this would allow the glass to re-flow and reduce number and size of the defects. Also, by annealing, the roughness of the waveguide walls could be reduced. However, the glass transition temperature is in excess of 1200 °C, and annealing of the films would be difficult. The best solution would be to eliminate the cause of the defects by suitably modifying the fabrication process. Surface roughness is a possible cause of defects since film deposition on a rough or dirty surface may result in voids from incomplete

coverage or shadowing. The surface roughness could have been caused by incomplete removal of photoresist or dust particles. Another possibility, although much less likely, was that the defects were caused by the PECVD deposition process (homogeneous nucleation, improper stoichiometry or temperature stresses). More investigation and experimentation will have to be done before the cause is found.

4.3 Practical Considerations Before Commercialization

In order to commercialize the sensor, many production issues must be addressed. For example, suitable packaging and assembly of the device must be addressed. As detailed in the previous section, polymer optical adhesive is not be a viable material for cementing the fibres to the waveguides. A mechanical aid might be used. V-grooves etched in silicon are often used as alignment aids, however, silicon cannot be used in a microwave environment because arcing and melting of the silicon would occur. If a trench is made or ridges formed in the glass such that little or no horizontal motions was possible and if the optical fibres were inserted in the trench with optical adhesive, then there would be less of an opportunity for the fibre to move. This configuration is impractical because the fibre cladding is 125 µm in diameter, and almost 62.5 µm of material would have to be etched away. A better method might be to first grind the fibre into a D-shape and then etch only 10 µm of material away. Figure 4.2 illustrates the fibre attachment

configuration.

Other practical considerations relate to the performance of the sensor. Although a response time of 80 seconds may be adequate when the sensor is used as a process monitoring instrument, the response time must lowered to the sub-second range, otherwise it would be impractical to use as a hand held wand-type sensor. There are a number of methods of decreasing the response time. One method would be to determine the optimum size of the susceptor. Its width, height and thickness could be optimized for improved heat transfer.

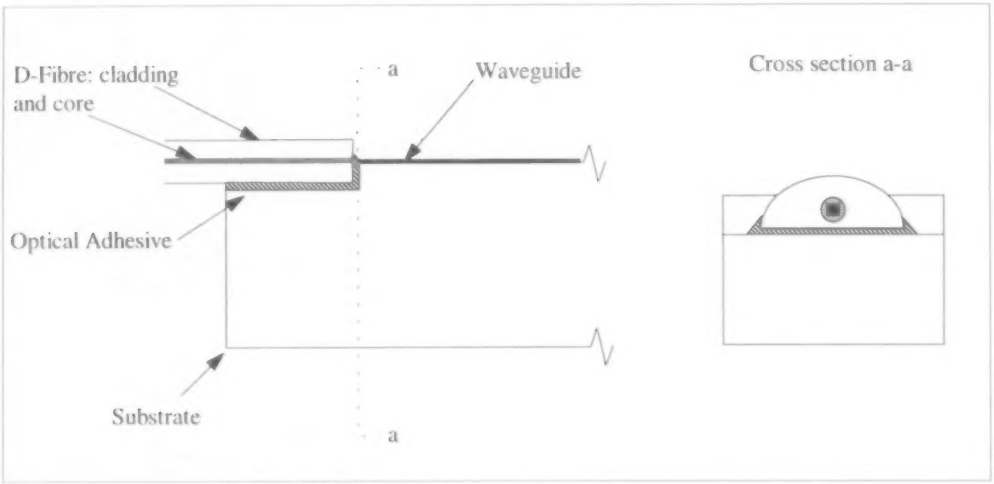

Figure 4.2 Improved method of butt coupling the fibres to the waveguides.

The final difficulty that must be addressed is packaging. The current sensor package is not robust enough to be used as a practical device. The

sensor could be enclosed in a low loss dielectric, such as a quartz tube. A small amount of optical adhesive may be used to cement the sensor inside the tube to prevent it from moving within the tube. The ends of the tube could be sealed by heating the tube above its glass transition temperature and then sealing the end. This type of package would also be useful if the sensor were to be used as a hand held wand-type instrument, because the quartz tube could be bent to any shape and cut to the appropriate size for each application. It is likely that a number of packages would be developed, each suited to a different application and environment, for commercialization.

4.4 Future Work and Directions

There are a number of avenues of improvement for the current design. Two such possible designs modifications which will be discussed are: replacement of the input MMI coupler with a symmetrical centre fed coupler and replacement of the output 2x2 MMI coupler with a 2x4 MMI coupler.

As mentioned earlier in Section 2.4, the imbalance caused by unequal splitting and re-combination (i.e. the tap ratios k_{tx} not being equal to 0.5) of the light limits the optical dynamic range of the device. If a symmetric MMI coupler were used at the input instead of a general MMI coupler, the imbalance would be greatly improved. Since the coupler is symmetrical, the main source of imbalance would be the misalignment of the input and output access waveguides defined by the photolithography step. The symmetric

MMI coupler has been shown to improve the power balance in simulations. The imbalance of the symmetrical MMI was calculated to be 0.02 dB while the original design was calculated to be 0.1 dB according to the simulation data. A third prototype has already been designed and the mask has been received. Fabrication will begin as soon as possible.

A second design improvement that may be pursued involves replacing the output 2x2 coupler with a 2x4 coupler. With the 2x2 MMI coupler, outputs 1 and 2 are complements of one another, i.e., when output 1 is maximum output 2 is a minimum. Hence, one channel becomes somewhat redundant. The only advantage of having access to both outputs is that the total power can be calculated and used as a normalization for both outputs. Implementing the normalization technique would reduce the effect of the varying input power caused by the input fibre moving from heating of the optical adhesive. If a two-in-four-out output coupler were used, then quadrature, or phase, information could be obtained. Each output experiences 4-beam interference. The result is that the MZ intensity transfer function at each output is shifted by 90°, relative to adjacent output channels (see Figure 4.3).

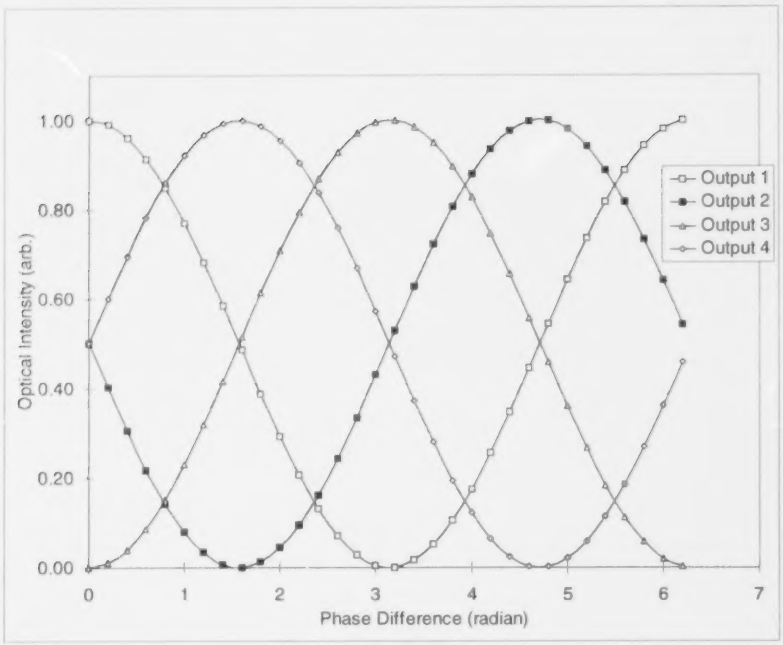

Figure 4.3 Intensity at the output of a 2x4 MMI coupler.

Acquiring the phase information is important; to extend the optical dynamic range of the sensor. With this phase information it is possible to eliminate phase ambiguity. For this reason, prototypes I and II can only operate over *one half* of a MZ period. If a 2x4 coupler was used, then the phase at any point could be determined. Not only could the sensor operate over a complete period, but fringe or peak counting could be used. Fringe counting is difficult, requires extra computation and calibration problems can occur if the sensor is not initialized properly. Even if the fringe counting is not used, using a 2x4 coupler will increase the dynamic range of the device by a factor of two. The tradeoff requires only a moderate design change and the added

difficulty of attaching five fibres rather than three.

In this chapter some of problems, such as poor response time and fibre to waveguide coupling, have been discussed. Comparisons between the modeled results and experimental results were attainable only for the optical model. The heat transfer and microwave interaction models require precise knowledge of certain material properties, such as thermal conductivity, microwave loss factor, and others. Furthermore, knowledge of these properties as a function of temperature must also be obtained before suitable predictions are possible. Future designs that incorporate symmetrical input couplers and 2x4 output couplers will most certainly improve the overall performance of the sensor.

5. CONCLUSION

The design and fabrication of an integrated optic microwave power sensor has been presented. It has been demonstrated that the sensor is capable of responding to low (25 W) and very high power levels (>900 W), resulting in a large dynamic range and high sensitivity. The sensor is capable of measuring microwave power at a point in space which facilitates the determination of the power distribution inside a microwave cavity. Also, successful integration of well balanced multimode interference couplers has resulted in the ability to integrate a Mach-Zehnder interferometer and a susceptor into a single device.

Although the work in this thesis has carried the project from the design stage to the fabrication and testing stages, further work is necessary before a practical product is available. Specifically, the connection between the optical fibres and the sensor waveguides is cumbersome and unreliable. Measures can be taken to reduce the effects of dynamic coupling variations between the waveguide and fibres, and will likely include signal processing. The best direction to pursue, however, is to investigate better methods of coupling the fibres to the waveguides, because it is this link which is the most vulnerable in the sensing system.

REFERENCES

[1] J. Dakin & B. Culshaw, *Optical fiber sensors: Principles and components*, Artech House, 1988

[2] B. Schmauβ, M. März, & J. Ernst, *"A fiber-optic sensor for microwave field measurement,"* Review of Scientific Instruments, vol. 66, 1995, pp. 4031 - 4033

[3] K. A. Wickersheim, et al, *"Fiberoptic techniques for measuring the magnitude of local microwave fields and power,"* U.S. Patent #5,110,216, 1992

[4] M. Dagys, Z. Kancleris, V. Orsevskis, & R. Simniskis, *"Resistive sensor for high power short pulse microwave measurement in waveguides,"* Electronics Letters, vol. 31, 1995, pp. 1355 - 1357

[5] F. Roussy, K. Agbossou, B. Dichtel, & J-M Thiebaut, *"High electromagnetic field measurements in industrial applicators by using an optically modulated sensor,"* J. Microwave Power and Electromagnetic Energy, vol. 27, 1992, pp. 164 - 170

[6] P. S. Apté & W. D. MacDonald, "*Microwave sintering kilogram batches of silicon nitride*," Ceramic Transactions, vol. 59: Microwaves: Theory and application in materials processing III (D. E. Clark, D. C. Folz, S. J. Oda, & R. Silberglitt, eds.), 1995, pp. 49 - 62

[7] S. J. Oda, "*Microwave applications to process nuclear and hazardous waste*," Ceramic Transactions, vol. 36: Microwaves: Theory and applications in materials processing II (D. E. Clark, W. R. Tinga, J. R. Laia, eds) 1993, pp. 73 - 79

[8] B. Saleh & M. Teich, Photonics, J. Wiley & Sons, 1991

[9] D. M. Pozar, Microwave Engineering, Addison-Wesley Publishing Co., 1993

[10] D. W. Hess, "*Plasma-enhanced CVD: Oxides, nitrides transition metals, and transition metal silicides*", J. Vacuum Technology, vol. 2, 1984, pp. 244 - 251

[11] E. P. G. T. van de Ven, "*Plasma deposition of silicon dioxide and silicon nitride films*", Solid State Technology, April 1981, pp. 167 - 171

[12] J. P. Simko & G. S. Oehrlein, *"Reactive ion etching of silicon and silicon dioxide in CF_4 plasmas containing H_2 and C_2F_4 additives"*, J Electrochemical Society, vol. 138, 1991, pp. 2748 - 2752

[13] T. Tamir, Integrated optics, 2nd ed., Topics in applied physics, vol. 7, Chapter 2, 1982

[14] A. Kumar, D. F. Clark, & B. Culshaw, *"Explanation of errors inherent in the effective-index method for analyzing rectangular-core waveguides,"* Optics Letters, vol. 13, 1988, pp. 1129 - 1131

[15] A. S. Sudbø, *"Why are accurate computations of mode fields in rectangular dielectric waveguides difficult?,"* IEEE J. Lightwave Technology, vol. 10, 1992, pp. 418 - 419

[16] R. März, Integrated optics, Artech House, 1995, Chapter 4

[17] E. Anemogiannis & E. N. Glytsis, *"Multilayer waveguides: Efficient numerical analysis of general structures,"*, IEEE J. Lightwave Technology, vol. 10, 1992, pp. 1344 - 1351

[18] M. Taylor, *FWave*: Software for determining electric field distribution in channel waveguide, 1996, public domain

[19] M. N. O. Sadiku, Numerical techniques in electromagnetics, CRC Press, 1992, pp. 179 - 188

[20] K. S. Yee, *"Numerical solution of initial boundary-value problems involving Maxwll's equations in isotropic media,"* IEEE Transaction of Propagation, vol. 14, 1966, pp. 302 - 307

[21] D. S. Katz, E. T. Thiele & A. Taflove, *"Validation and extension to three dimensions of the Berenger PML absrobing boundary condition for FD-TD meshes"*, IEEE Microwave and Guided Wave Letters, vol. 4, 1994, pp. 268 - 270

[22] L. B Soldano & E. C. M. Pennings, *"Optical multi-mode interference device based on self-imaging: Principles and applications,"* IEEE J. Lightwave Technology, vol. 13, 1995, pp. 615 - 627

[23] N. Kapany & J. Burke, *Optical Waveguides*, Academic Press, 1972

[24] L. B. Soldano et al., *"Planar monomode optical couplers based on multimode*

interference effects," IEEE J. Lightwave Technology, vol. 10, 1992, pp. 1843 - 1849

[25] P. A. Besse, M. Bachmann, H. Melchior, L. B. Soldano, & M. K. Smit, *"Optical bandwidth and fabrication tolerances of multimode interference couplers,"* IEEE J. Lightwave Technology, vol. 12, 1994, pp. 1004 - 1009

[26] J. N. McMullin, *"Explicit split-step propagating beam method"*, IEEE Photonics Technology Letters, vol. 6, 1994, pp. 534 - 536

[27] A. Kunz, F. Zimulinda, & W. E. Heinlein, *"Fast three-dimensional split-step algorithm for vectorial wave propagation in integrated optics"*, IEEE Photonics Technology Letters, vol. 5, 1993, pp. 1073 - 1076

[28] M. Rivera, *"A finite difference BPM analysis of bent dielectric waveguides"* IEEE J. Lightwave Technology, vol. 13, 1995, pp. 233 - 238

[29] E. Udd, Fifber optic sensors, Wiley & Sons, 1991, pp. 275 - 276

[30] R. A. Rudder et al., *"Diamond chemical vapor deposition vi microwave excited plasma from water-ethanol* solutions", Ceramic Transactions, vol. 36:

Microwaves: Theory and applications in materials processing II (D. E. Clark, W. R. Tinga, J. R. Laia, eds) 1993, pp. 377 - 384

[31] A. C. Metaxas & J. Meredith, Industrial microwave heating, Peter Peregrinus, 1993, pp. 122 - 123

[32] M. Ohring, The materials science of thin films, Academic Press, 1992

APPENDIX I

Additional calculations for a mirrored image about the x-axis in an MMI

The field distribution as a function of x and $z=L_{s,p}$ in the MMI is given by:

$$\Phi\left(x, L_{s,p}\right) = A\sum_{v=0}^{N-1} c_v \sin\left(\frac{\pi x(v+1)}{W}\right) e^{j\pi v(v+2)\frac{s}{p}} \tag{A.1}$$

If $\sin(x) = \frac{e^{jx} - e^{-jx}}{j2}$ and s=p=1, then

$$\Phi\left(x, L_{1,1}\right) = \frac{A}{j2}\sum_{v=0}^{N-1} c_v \left\{ e^{\frac{j\pi x(v+1)}{W}} - e^{\frac{-j\pi x(v+1)}{W}} \right\} e^{j\pi v(v+2)} \tag{A.2}$$

$$\Phi\left(x, L_{1,1}\right) = \frac{A}{j2}\sum_{v=0}^{N-1} c_v \left\{ e^{j\pi\left[\frac{x(v+1)+v(v+2)W}{W}\right]} - e^{j\pi\left[\frac{x(v+1)-v(v+2)W}{W}\right]} \right\} \tag{A.3}$$

$$\Phi\left(x, L_{1,1}\right) = \frac{A}{j2}\sum_{v=0}^{N-1} c_v \left\{ e^{-j\pi\left[\frac{x(v+1)(W-x)}{W}\right]} e^{-j\pi\left(v^2+3v+1\right)} - e^{j\pi\left[\frac{x(v+1)(W-x)}{W}\right]} e^{j\pi\left(v^2+3v+1\right)} \right\} \tag{A.4}$$

$$\Phi\left(x, L_{1,1}\right) = A\sum_{v=0}^{N-1} c_v \sin\left(\frac{(v+1)(W-x)}{W}\right) \tag{A.5}$$

The following equation describes an image of the input field that has been mirrored about the x-axis.

$$\Phi\left(x, L_{1,1}\right) = A\sum_{v=0}^{N-1} c_v \Phi(W-x) \tag{A.6}$$